

## Article

# Genesis of Rare Metal Granites in the Nubian Shield: Tectonic Control and Magmatic and Metasomatic Processes

Mohamed Zaki Khedr <sup>1,\*</sup>, Saif M. Abo Khashaba <sup>1</sup>, Eiichi Takazawa <sup>2</sup>, Safaa M. Hassan <sup>3</sup>, Mokhles K. Azer <sup>4</sup>, N. H. El-Shibiny <sup>1</sup>, Kamal Abdelrahman <sup>5</sup> and Yuji Ichiyama <sup>6</sup>

<sup>1</sup> Geology Department, Faculty of Science, Kafrelsheikh University, Kafrelsheikh 33516, Egypt

<sup>2</sup> Geology Department, Faculty of Science, Niigata University, Niigata 950-2181, Japan

<sup>3</sup> National Authority for Remote Sensing and Space Sciences (NARSS), Cairo 1564, Egypt

<sup>4</sup> Geological Sciences Department, National Research Centre, Cairo 12622, Egypt

<sup>5</sup> Department of Geology and Geophysics, College of Science, King Saud University, P.O. Box 2455, Riyadh 11451, Saudi Arabia

<sup>6</sup> Graduate School of Science, Chiba University, Chiba 263-8522, Japan

\* Correspondence: mohamed.khader1@sci.kfs.edu.eg; Fax: +2-047-264-6545

**Abstract:** The Igla Ahmr region in the Central Eastern Desert (CED) of Egypt comprises mainly syenogranites and alkali feldspar granites, with a few tonalite xenoliths. The mineral potential maps were presented in order to convert the concentrations of total rare earth elements (REEs) and associated elements such as Zr, Nb, Ga, Y, Sc, Ta, Mo, U, and Th into mappable exploration criteria based on the line density, five alteration indices, random forest (RF) machine learning, and the weighted sum model (WSM). According to petrography and geochemical analysis, random forest (RF) gives the best result and represents new locations for rare metal mineralization compared with the WSM. The studied tonalites resemble I-type granites and were crystallized from mantle-derived magmas that were contaminated by crustal materials via assimilation, while the alkali feldspar granites and syenogranites are peraluminous A-type granites. The tonalites are the old phase and are considered a transitional stage from I-type to A-type, whereas the A-type granites have evolved from the I-type ones. Their calculated zircon saturation temperature  $T_{Zr}$  ranges from 717 °C to 820 °C at pressure < 4 kbar and depth < 14 km in relatively oxidized conditions. The A-type granites have high SiO<sub>2</sub> (71.46–77.22 wt.%), high total alkali (up to 9 wt.%), Zr (up to 482 ppm), FeOt/(FeOt + MgO) ratios > 0.86, A/CNK ratios > 1, Al<sub>2</sub>O<sub>3</sub> + CaO < 15 wt.%, and high ΣREEs (230 ppm), but low CaO and MgO and negative Eu anomalies (Eu/Eu\* = 0.24–0.43). These chemical features resemble those of post-collisional rare metal A-type granites in the Arabian-Nubian Shield (ANS). The parent magma of these A-type granites was possibly derived from the partial melting of the I-type tonalitic protolith during lithospheric delamination, followed by severe fractional crystallization in the upper crust in the post-collisional setting. Their rare metal-bearing minerals, including zircon, apatite, titanite, and rutile, are of magmatic origin, while allanite, xenotime, parisite, and betafite are hydrothermal in origin. The rare metal mineralization in the Igla Ahmr granites is possibly attributed to: (1) essential components of both parental peraluminous melts and magmatic-emanated fluids that have caused metasomatism, leading to rare metal enrichment in the Igla Ahmr granites during the interaction between rocks and fluids, and (2) structural control of rare metals by the major NW–SE structures (Najd trend) and conjugate N–S and NE–SW faults, which all are channels for hydrothermal fluids that in turn have led to hydrothermal alteration. This explains why rare metal mineralization in granites is affected by hydrothermal alteration, including silicification, phyllic alteration, sericitization, kaolinitization, and chloritization.

**Keywords:** Nubian Shield; rare metal-bearing granites; mineral chemistry; hydrothermal alterations; machine learning; Egypt



**Citation:** Khedr, M.Z.; Abo Khashaba, S.M.; Takazawa, E.; Hassan, S.M.; Azer, M.K.; El-Shibiny, N.H.; Abdelrahman, K.; Ichiyama, Y. Genesis of Rare Metal Granites in the Nubian Shield: Tectonic Control and Magmatic and Metasomatic Processes. *Minerals* **2024**, *14*, 522. <https://doi.org/10.3390/min14050522>

Academic Editor: Martiya Sadeghi

Received: 19 April 2024

Revised: 10 May 2024

Accepted: 13 May 2024

Published: 17 May 2024



**Copyright:** © 2024 by the authors. Licensee MDPI, Basel, Switzerland. This article is an open access article distributed under the terms and conditions of the Creative Commons Attribution (CC BY) license (<https://creativecommons.org/licenses/by/4.0/>).

## 1. Introduction

Granitic rocks are the main constituent of the continental crust and can be classified into S-, I-, and A-types based on their chemical features (e.g., [1–5]). These granite types may reflect the tectonic regime in which they were formed [1–5]. The I- (subduction-related) and A-type (anorogenic) granites are widespread in the Arabian-Nubian Shield (ANS) and show different mineralogical and geochemical compositions [3–9]. The post-collisional granites can refer to geodynamic evolution of the ANS because they represent a major mass addition to the upper juvenile continental crust [6–10]. They are highly fractionated or evolved, highly silicified (high in silica), and crystallized from peraluminous magmas. The post-collisional granites also have an economic interest because they are highly enriched in both rare earth elements (REEs > 200 ppm) and high field strength elements (HFSEs); these REEs and HFSEs are possibly controlled by parent magmatic compositions and fractionation processes [4–7,11]. Furthermore, most ANS granites are affected by post-magmatic processes, including greisenization, albitization, microclinization, muscovitization, sericitization, kaolinitization, silicification, and chloritization. These metasomatic processes and hydrothermal alteration increase the rare metal contents and are essential to their accumulation [2–11].

The rare metal granites in the ANS have received much attention from economic geologists due to their substantial potential as sources of REEs, Nb, Au, Li, Ta, Sn, W, Mo, U, Zr, and Th [12–14]. They are mainly distributed in definite zones in the Central Eastern Desert (CED) and in the northern border of the Southern Eastern Desert (SED) of Egypt in fourteen localities (Supplementary Figure S1), including (1) Umm Naggat, (2) Umm Samra, (3) Abu Dabbab, (4) Nuweibi, (5) Ineigi, (6) Homrit Waggat, (7) Igla (or Igla Ahmr; this study), (8) Zabara, (9) Mueilha, (10) Nugrus, (11) El-Gharabiya, (12) Nikeiba, (13) Homrit Akarem, and (14) Um Hibal [4–7,9,11,13,15,16]. The high rare metal content in these fourteen mineralized granite plutons is not haphazard, but it was possibly controlled by structural trends (mainly NW–SE of the Najd fault) and the magma composition of granitic plutons [7,8]. Therefore, it is important to determine the magma sources and melting conditions of mineralized granites in the ANS, and to understand the mechanism of rare metal enrichment during magmatic versus metasomatic processes. According to previous studies, highly fractionated granites are enriched in rare metals and REEs (>500 ppm) relative to less fractionated or evolved ones [17–19]. The evolved REE- and HFSE-rich granites can be classified either as highly fractionated I-type [20] or A-type granites [19].

Machine learning algorithms (MLAs), which comprise artificial neural networks (ANNs), regression trees (RTs), random forests (RFs), and support vector machines (SVMs), are widely used in mineral prospectively [21–23]. MLAs have the potential to recognize and simulate the intricate non-linear correlations between mineral occurrences and evidencing aspects [24]. These methods are capable of handling a broad variety of evidential characteristics that could be essential in prospective mineral research. The model becomes unacceptable to overfitting due to the curse of dimensionality; however, more input evidential features may result in higher complexity and bigger numbers of model parameters [21]. It is used for the first time in delineating a potential map of rare metal-bearing granites in Egypt. This model was applied to the Igla Ahmr granite pluton, which is one of the best plutonic intrusions of rare metal granites in the ANS [8].

The Igla Ahmr rare metal-bearing granites (this study) are considered the older phase of the mineralized granites in the ANS and formed at 679–691 Ma [9]. The NW–SE and N–S structural trends are dominant in the Igla Ahmr granite pluton and possibly control the distribution of the rare metal mineralization [8]. This study deals with remote sensing, mineral chemistry (major and trace elements), and whole-rock compositions of granitic rocks from the Igla Ahmr area to unravel the origin and evolution of the mineralized granites and to understand factors controlling rare metal mineralization. Our study aims to explain why rare metal-bearing granites are distributed in a particular region or zone of the Eastern Desert of Egypt and why some plutons are mineralized but most are not.

Remote sensing and geochemical data may shed light on the role of the Najd fault system in concentrations of rare metal-bearing granites in a specific region in the Eastern Desert of Egypt. Using machine algorithms like weighted overlay and random forest are crucial for outlining the rare metal potential maps in the Iгла Ahmr region. This study also gives evidence for the consistent relationship between the rare metal enrichment in the Iгла Ahmr granites and both granitic magma composition and associated hydrothermal activity.

## 2. Regional Geology and Location of the Study Area

The Iгла Ahmr area covers an area of about ~307 km<sup>2</sup> in the Central Eastern Desert (CED) of Egypt as part of the northern region of the ANS (Figure 1a,b), which is the northern part of the East African Orogen (EAO) and composed mainly of the juvenile Neoproterozoic crust [25]. This area lies at 10 Km NW of Marsa Alam City. The Iгла Ahmr area is bound by latitudes 25°04'N to 25°17'N and longitudes 34°35'E to 34°45'E (Figure 1a,b), and is one of Egypt's fourteen mineralized granite plutons (Supplementary Figure S1). The distribution of mineralized granites in the Homrit Waggat, Nuweibi, Abu Dabbab, and Umm Naggat areas is mainly in a certain zone in the CED and close to the Iгла Ahmr mineralized granites (Figure 1a), while the Sikait and El-Hima mineralized granites are found in the northern border of the South Eastern Desert (SED) [5–9,12–16]. All these granites and their rare metal deposits were structurally controlled by NW–SE and N–S trends [5–9,12–16,26–28] (Figure 1a). The NW-trending tectonic fabric is dominant in the CED, where the transpressional-related NW sinistral shear was conjugated with the predominant dextral transpression along the NE–SW shear zone associated with N–S faults [26–28] (Figure 1a). The Iгла Ahmr area occurs 10 km north of the major E–W dextral strike fault that extends along the Idfu-Marsa Alam asphaltic road (Figure 1a). The Neoproterozoic rocks exposed in the Iгла Ahmr area comprise ultramafic rocks (e.g., serpentinites), mafic metavolcanic rocks, metasediment, metagabbro-diorite plutons, and granitoid rocks (Figure 1b). Therefore, the geology of the Iгла Ahmr area is commonly described according to three major tectonostratigraphic units, from the oldest to the youngest unit: (1) dismembered ophiolite and ophiolitic mélangé, (2) island arc associations (e.g., metasediment), and (3) syn- to post-orogenic gabbroic to granitic intrusions. All rocks in the Iгла Ahmr area were affected by two major sets of faults, showing NW–SE and N–S trends (Figure 1b). This resembles the geology and structure of the CED, where the crustal rocks and ophiolite in the CED were intruded by syn-tectonic granite and a series of late to post-tectonic mineralized granites [28]. The NW–SE structural trend is attributed to the major NW-trending sinistral shear zones of the Najd fault system (640–540 Ma ago; [28]). The Iгла Ahmr granitoid stocks are considered the south extension of the highly enriched rare metal-bearing granites in the Abu Dabbab area (Figure 1a) that was affected with the NW–SE trending (3-km-wide, 15-km-long) fault, forming the Wadi Abu Dabbab shear zone [28]. The Iгла Ahmr granitoid stocks are cut by dykes and aplite veins, which take the same trend (NW–SE) as that of the faults in the studied area.

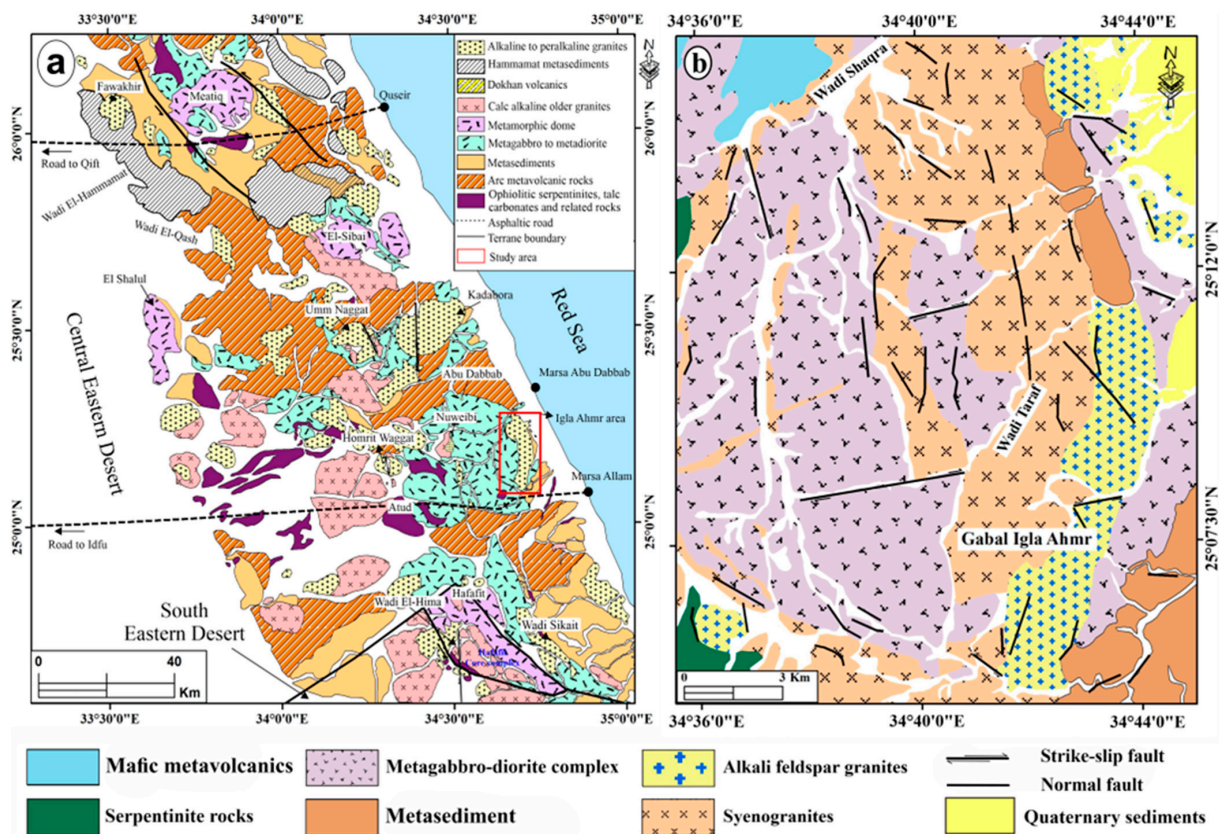


**Figure 1. (a)** Geological map of the Eastern Desert of Egypt showing the distribution of rare meta-bearing granites [29]. **(b)** The geological map of the Iqla Ahmr area produced from the combination of remote sensing images, field study, petrography, and geological maps modified after the Egyptian Geologic Survey and Mining Authority [8,30]. The structure and tectonic fabric trends in panel (a) are compiled from Greiling et al. [26], Fritz et al. [27], and Abd El-Wahed [28].

### 3. Remote Sensing Data and Methods

The data layers or evidential maps used in this study were derived from four datasets: lithology, structure, ASTER alteration indices, and geochemistry. The geological map (Figure 1a,b) used in this study was derived from the accurate discrimination of lithological rock units integrating remote sensing, field investigation, and petrography [8]. The structural features were detected using Sentinel-1 radar data [8]. ASTER data were used as the third dataset, which was processed after correction [8]. Five evidential maps were produced from ASTER images as an alteration index ( $b_4/b_5$ ) that emphasizes several alteration zones, phyllic alteration ( $b_5 + b_7/b_6$ ),  $Fe^{+2}$  - Si alteration ( $b_5/b_4$ ), propylitic alteration ( $b_7 + b_9/b_8$ ), and hydroxyl group index ( $b_7/b_6 \times (b_4/b_6)$ ) (Supplementary Figure S2). Rare metal geochemical data using kriging interpolation were the last dataset used in this study (Supplementary Figure S2).

#### 3.1. Weighted Sum Model

In this study, extracting multi points to the raster tool have been applied as a preprocessing step using ArcGIS-pro version 3.0 to calculate each relative value for each cell of raster input data (evidence layer) (Supplementary Table S1). These values are added (as separate fields) to the geochemistry attribute layer of the rare metal concentrations. Then, an exploratory regression tool was applied in order to see the significance or importance of evidence layers. In addition, the significant weights for each data input were determined using the exploratory regression tool.

Based on the exploratory regression results, the weighted sum model has been applied using the 18-evidence layer with regard to the different weights (Supplementary Table S1).

By using the weighted sum model, the highest prospective areas related to rare metal mineralization appeared with a rose color (Figure 2), and the lowest prospective areas were discriminated with a red color (Figure 2). The total surface area was calculated and related to 10 classes of the analyzed rare metals prospective priority (REEs, Sc, Y, Zr, Th, U, Nb, Ta, Mo, and Ga), as well as five alteration indices and line density at the study area (Supplementary Figure S2).

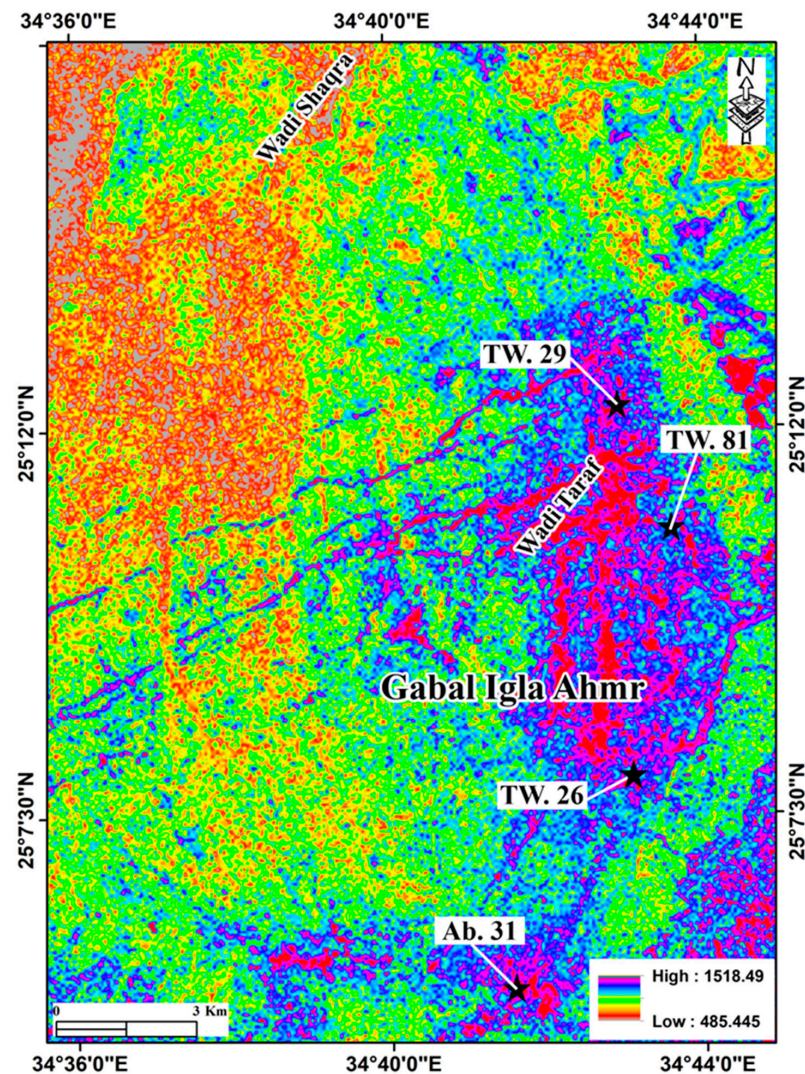


**Figure 2.** Weighted sum model showing the distribution of rare earth elements in the Iгла Ahmr area. Ab. 31, TW. 26, TW. 29, and TW. 81 are granite sample numbers enriched with REEs.

### 3.2. Random Forest-Based Classification and Regression

The forest-based classification and regression tool produces models and creates predictions using the adaptation of Leo Breiman's random forest algorithm that is a method of the supervised machine learning. Random forest (RF) is a set of classification and regression trees used for predictions [31,32]. It is possible to make predictions for continuous variables (regression) and categorical variables (classification). The form of fields in the attribute table of the training features shows explanatory variables. The predictions can be made for the features in addition to the validation of model performance in accordance with the training data [31,32]. Recently, RF is among the most widely used ensemble classifiers of rock units using remote sensing data [33].

The forest-based regression model is applied to predict the prospective rare metal enrichment (Figure 3). The highest prospective rare metal value is highlighted with red to

pink colors at alkali feldspar granites (Figure 3), while the map shows a range of blue to yellow colors at syenogranites (see geological map, Figure 1).

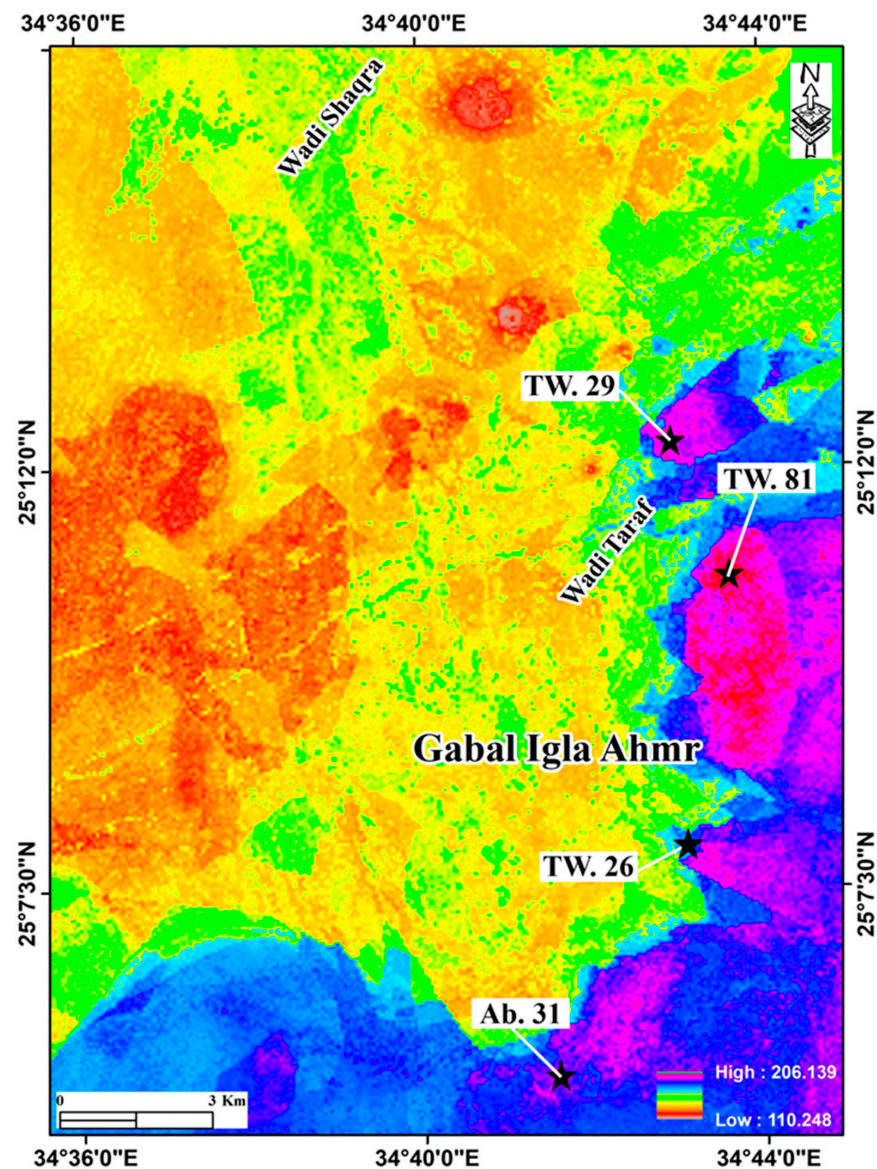
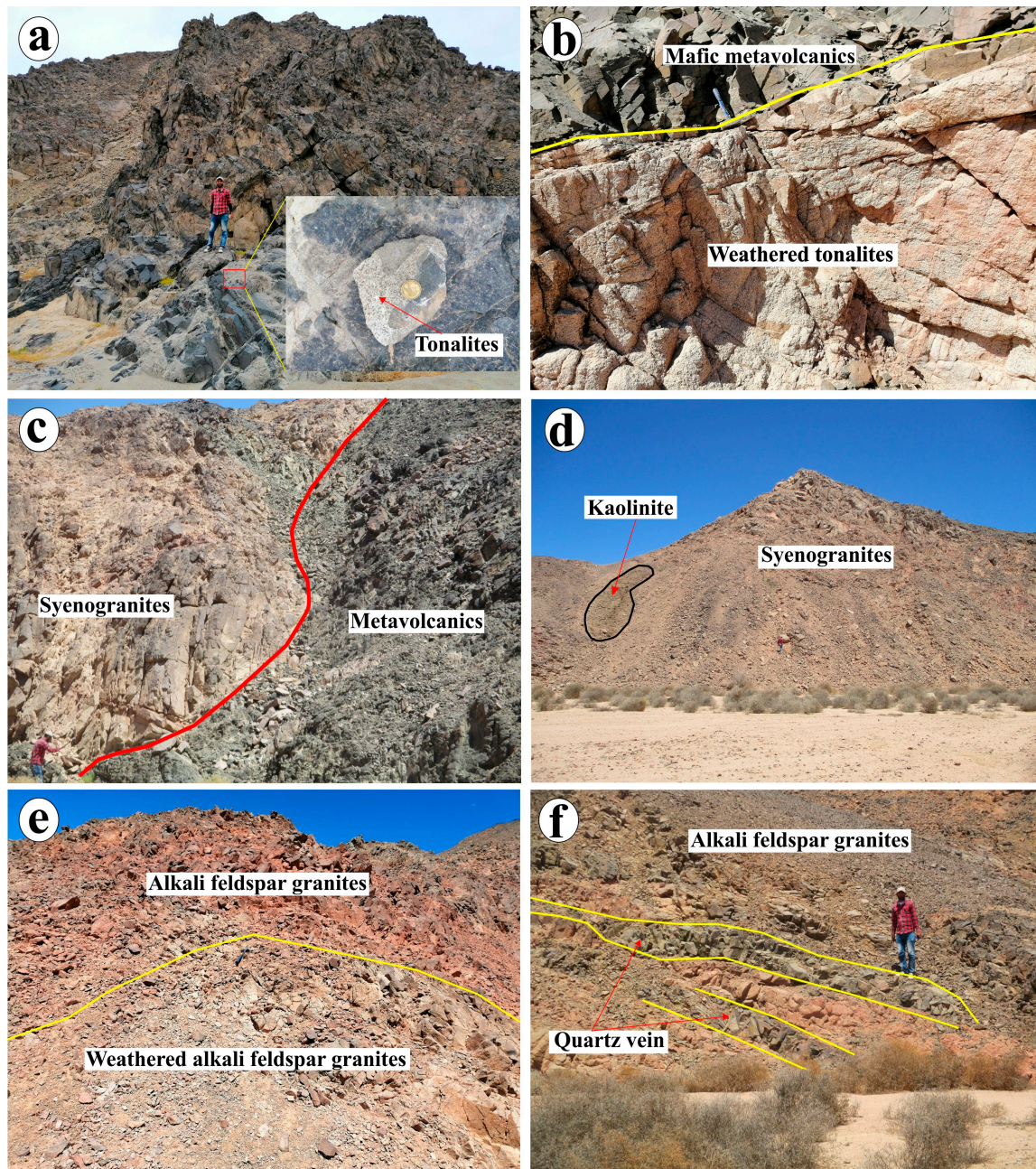


Figure 3. Random forest model showing the distribution of rare earth elements in the Iгла Ahmr area.

#### 4. Field Observation and Petrography

Granitoid rocks and their related altered samples (120 samples) were mainly collected based on remote sensing and field studies for laboratory studies. The Iгла Ahmr granitic pluton is composed of syenogranites and alkali feldspar granites with few tonalite xenoliths (Figures 1b and 4a–f). These tonalite xenoliths occur as very low relief in syenogranites and/or at the contact with metavolcanics at the northwestern part of the studied area, forming a sharp contact with metavolcanics (Figure 4a,b). Syenogranites are found as an elliptical shape and form the majority of the Iгла Ahmr pluton (Figures 1b and 4c,d). Syenogranites are more abundant and cover 85 km<sup>2</sup> in area. They are coarse-grained, have high relief terrain, and show a pink color (Figure 4d). Syenogranites intruded into the metagabbro-diorite plutons and formed sharp contacts with serpentinite, metasediment, and mafic metavolcanic rocks (Figures 1b and 4c). The coarse-grained red alkali feldspar granites, which are roughly 15 km long, occur at the eastern margin of the studied pluton (Figure 4e,f). The gradational contact was recognized between the syenogranites and alkali

feldspar granites [8]. The sharp intrusive contact is dominant between the alkali feldspar granites and the metagabbro-diorite complex [8]. They are highly weathered at their bottom (Figure 4e) and cut by many quartz veins typically less than 50 cm wide (Figure 4f). These veins show the same NW–SE trends as fractures and faults in the investigated area (Figures 1d and 4f). The studied granites suffered from various types of alteration, such as kaolinitization (Figure 4e), silicification (Figure 4f), and phyllic alteration.



**Figure 4.** Field photographs of the Igla Ahmr granites. (a) Tonalites intruded by mafic dykes. (b) The intrusive sharp contact between weathered tonalites and mafic metavolcanics. (c) The sharp intrusive contact between syenogranites and metavolcanics. (d) Kaolinite alteration in syenogranites. (e) Close-up view of the contact between fresh and weathered alkali feldspar granites. (f) High silicification and formation of quartz vein cutting alkali feldspar granites.

The nomenclature of granites is not only based on geochemistry but also based on point counting of modal volume% of their minerals and petrographic description of textures

(Figure 5) under polarized and reflected microscopy. Scanning electron microscopy (SEM) energy dispersive X-ray spectroscopy (EDS) with petrographic description was used to identify accessory minerals; please refer to Supplementary Figure File for further information on the analytical method. The Igla Ahmr granite pluton includes rare metal-bearing minerals such as zircon, rutile, allanite, xenotime, and parisite. Additionally, stream sediment derived from granites include zircon ( $ZrSiO_4$ ), monazite ( $(Nd, Ce, La, Th)(P, Si)O_4$ ), and betafite ( $(Ca, U)_2(Ti, Nb, Ta)_2O_6(OH)$ ) (Supplementary Table S2; Figures 6 and 7). The EDS spectrum and SEM images indicate the morphology of rare mineral grains and their distribution with other major silicate minerals. The rare metal-bearing minerals are accumulated around both Fe-Ti oxides (ilmenite and titanite; Figures 6a–d and 7b–d) and the K-rich phases such as biotite and K-feldspar (Figure 7c,d) as well as chlorite (Figure 6d). Allanite is intergrown with titanite and includes high Ti contents from the latter (Figure 7d). Betafite is heterogeneous in color and cracked due to the effect of hydrothermal alteration, suggesting a secondary origin (Figure 7e).

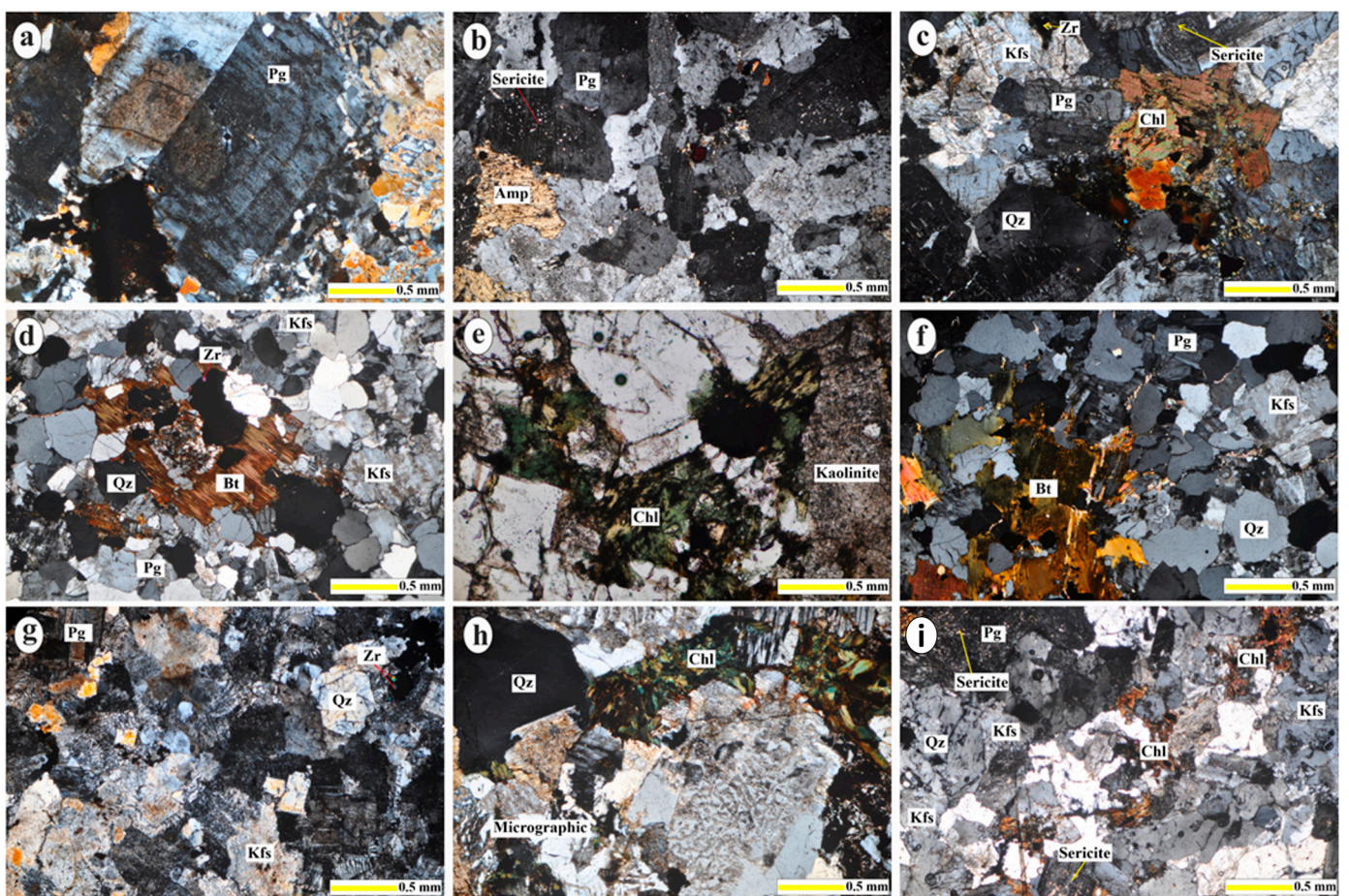


**Figure 5.** Photomicrographs images of the Igla Ahmr granites. (a) Plagioclase (Pg) crystal exhibiting normal zoning in the tonalites. (b) Coarse subhedral crystals of plagioclase (Pg) altered to sericite and associated with anhedral crystals of amphibole (Amp) in tonalites. (c) Chlorite flaky after biotite crystals filling interstitial spaces between primary silicates in syenogranite. (d) Small subhedral crystals of K-feldspar (Kfs) associated with large crystals of biotite flakes (Bt) in syenogranites. (e) Kaolinite and chlorite (Chl) alterations due to metasomatism, syenogranites. (f) Biotite (Bt) flaky existence as clots in interstitial between quartz (Qz) and feldspar in syenogranites. (g) Highly altered K-feldspar (Kfs) and plagioclase (Pg) in alkali feldspar granites. (h) Micrographic texture of intergrowth between fine-grained quartz and alkali feldspar in alkali feldspar granites. (i) Sericite alteration in the core of plagioclase (Pg) grains associated with chlorite (Chl) in alkali feldspar granites.

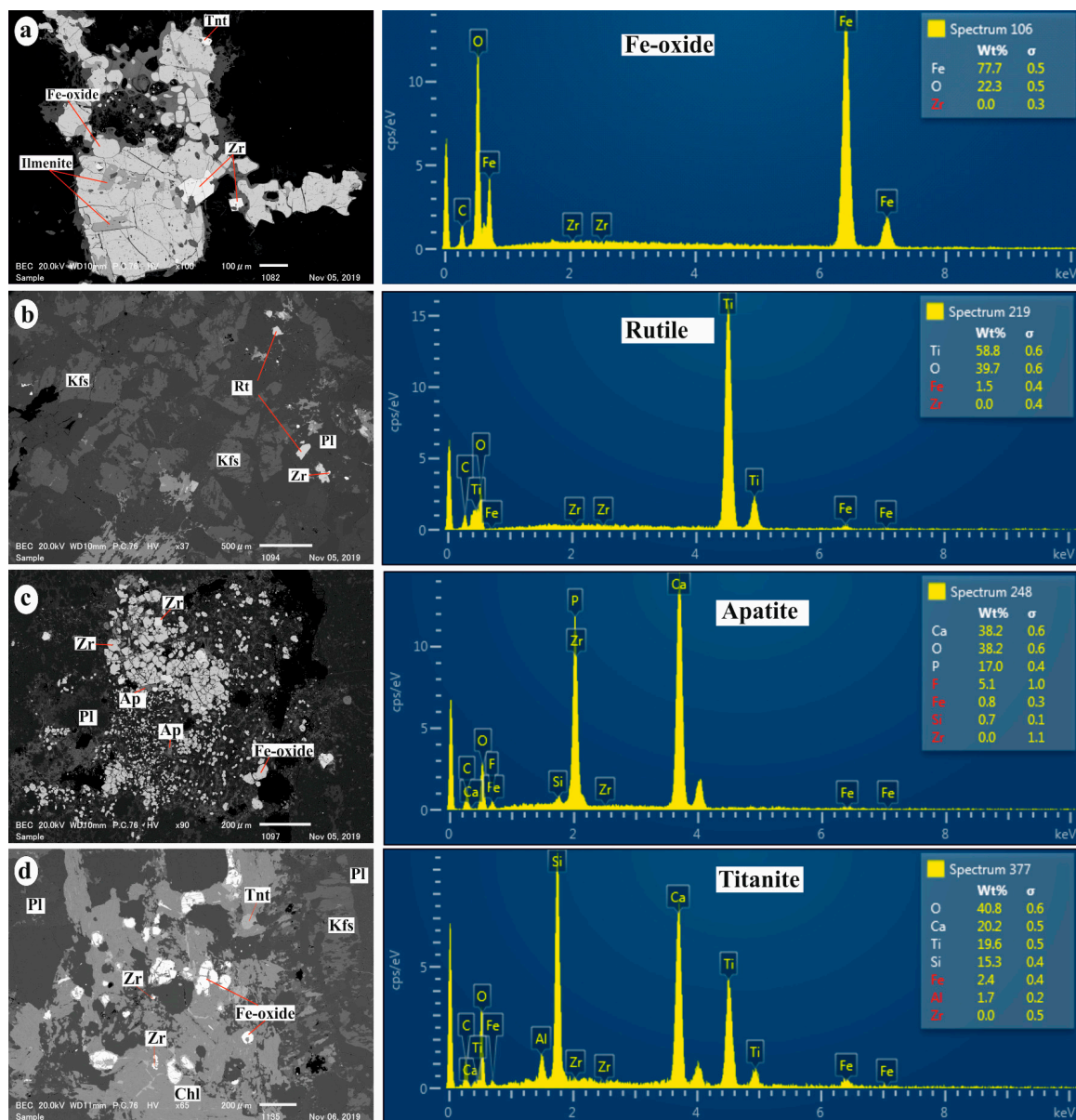


**Figure 6.** SEM images with EDS spectrum analyses of accessory minerals in the Igla Ahmr granites. (a) Coarse subhedral Fe-oxide crystals in alkali feldspar granites. (b) Tiny ilmenite crystals in plagioclase associated with zircon (Zr) in alkali feldspar granites. (c) Subhedral apatite crystals (Ap) accompanied with zircon (Zr) and Fe-oxide in alkali feldspar granites. (d) Small disseminated grains of titanite (Tnt) in alkali feldspar granites.

Tonalite xenoliths are coarse grained with a hypidiomorphic granular texture and consist mainly of plagioclase (50–60 vol.%), quartz (18–26 vol.%), K-feldspar (6–8 vol.%), biotite ~3 vol.%, chlorite ~2 vol.%, and hornblende ~1 vol.% (Figure 5a,b). Accessory minerals are Fe-Ti oxides, apatite, titanite, and zircon. Plagioclase occurs as subhedral to anhedral crystals (Figure 5a). Some plagioclase crystals show normal zoning (Figure 5b) and are sometimes altered to sericite and carbonate, mainly in the cores (Figure 5a,b). K-feldspar exists as anhedral crystals filling the interstitial spaces between the other silicates. Quartz interstitially exists as small anhedral crystals between plagioclase grains. Biotite is found as flakes or tabular crystals, which are partly altered to chlorite. Amphibole is found in the interstitial spaces between plagioclase crystals as small to medium-sized anhedral crystals (Figure 5b).

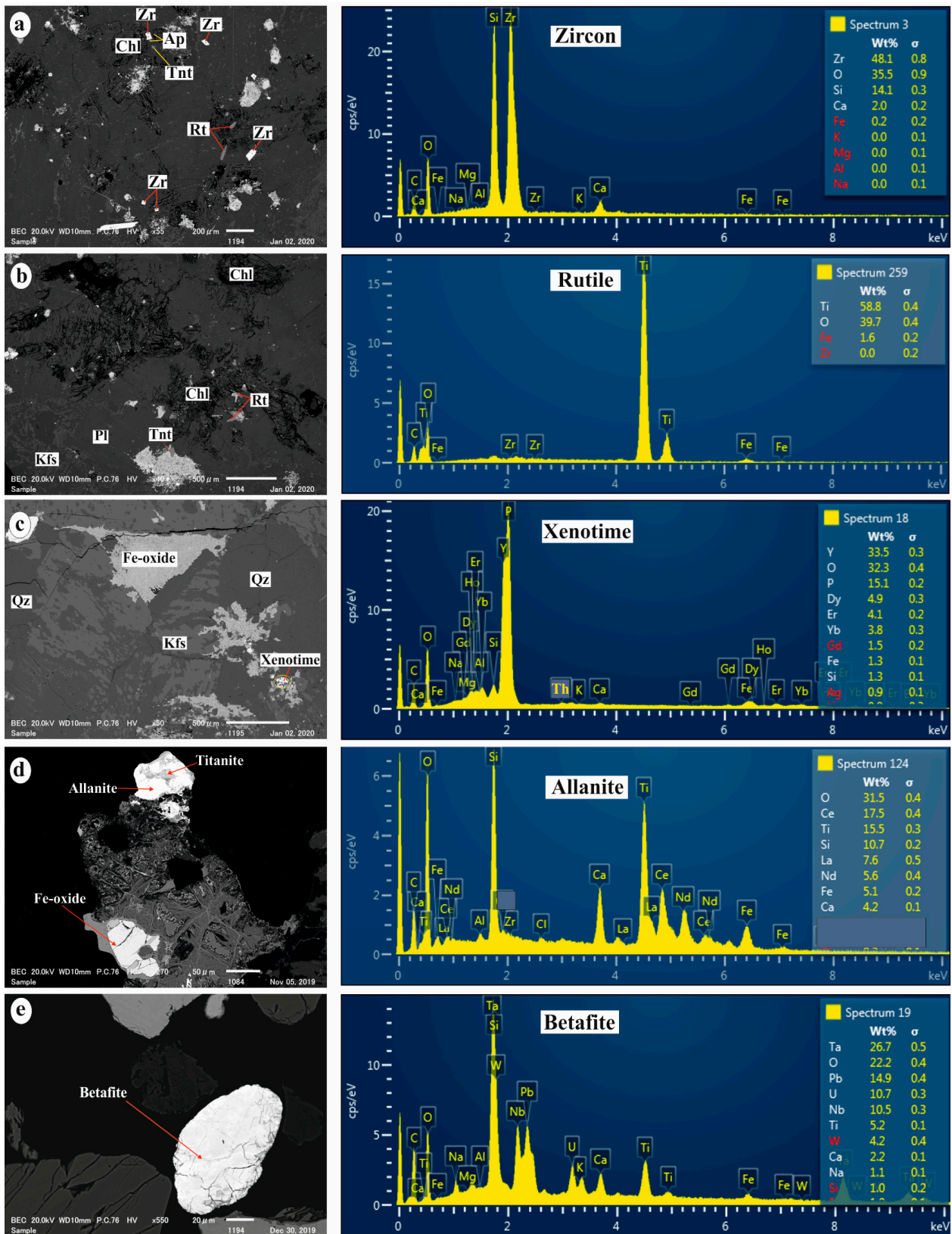


**Figure 7.** SEM images with EDS spectrum analyses of rare metal-bearing minerals in the Igla Ahmr alkali feldspar granites and stream sediments. (a) Subhedral zircon crystals associated with apatite, titanite, and chlorite in the silicate matrix. (b) Subhedral to euhedral rutile crystals. (c) Small anhedral grains of xenotime at the rim of Fe-oxide. (d) Titanite intergrowth with allanite as a composite grain at edge of iron oxide. (e) Betafite grains in stream sediments.

Syenogranites show hypidiomorphic granular textures and are essentially composed of K-feldspar (38–44 vol.%), quartz (25–35 vol.%), and plagioclase (15–25 vol.%) with subordinate biotite and muscovite (~1 vol.%) (Figure 5c–f). Epidote, amphibole, chlorite, kaolinite, and sericite are secondary minerals (1–2 vol.%) (Figure 5c–f). Accessory minerals (<2 vol.%) are euhedral zircon, Fe-Ti oxides, apatite, titanite, and xenotime (Figure 6a–d). Plagioclase occurs as prismatic crystals with albite twinning, while few crystals show normal zonation (Figure 5c–f). Few plagioclase crystals are altered to sericite in their core (Figure 5c–f). K-feldspars are found as subhedral to anhedral columnar crystals of perthite and microperthite (Figure 5c–f). Quartz forms sharp boundaries with other rock constituents and sometimes occurs as fine aggregated grains (Figure 5d,f). Biotite is found as interstitial flakes between quartz and feldspars and or as fine blades within the coarse crystals of feldspar (Figure 5d,f). It is converted to chlorite, mainly along the cleavage and crystal margins (Figure 5d). Muscovite exists as small flakes between plagioclase and quartz [8]. Apatite occurs as small needle-like crystals (Figure 5c), while Fe-oxide exists as euhedral crystals or as fine aggregated grains accompanied with altered biotite and chlorite (Figure 6d).

Alkali feldspar granites are pink to red in color and show a micrographic texture (Figure 5h). The main rock-forming minerals are K-feldspar (55–65 vol.%) and quartz (30–35 vol.%), with subordinate albite (6–10 vol.%), biotite, and muscovite (~1 vol.%) (Figure 5g–i) [8]. Chlorite, kaolinite, and sericite are secondary minerals (Figure 5g–i). The main accessory minerals are Fe-Ti oxides, zircon, titanite, rutile, xenotime, and apatite (Figures 6 and 7). Alkali feldspar comprises orthoclase, microcline, and perthite [8]. Anhedral crystals of quartz can occasionally intergrow into K-feldspar and plagioclase, forming a myrmekitic texture. The existence of a micrographic texture indicates the effect of hydrothermal fluids, causing hydrothermal alteration in the Igla Ahmr alkali feldspar granites. Plagioclase exists as subhedral columnar crystals and is usually corroded (Figure 5e). Plagioclase is mainly albite and oligoclase in composition and contains many apatite inclusions (Figures 5e and 6c; Supplementary Table S2). Biotite exists as coarse flakes and is generally altered to chlorite (Figure 5f) due to the hydrothermal alteration of the alkali feldspar granites. Biotite contains inclusions of zircon, ilmenite, and Fe-oxide, suggesting its primary origin. Amphibole is rare and occurs as subhedral plate crystals. Fe-oxide exists as anhedral to euhedral crystals and is usually associated with zircon, ilmenite, apatite, and xenotime (Figure 6a,c and Figure 7c). Zircon occurs as disseminated euhedral to subhedral crystals in chlorite and biotite (Figure 6a,b and Figure 7a); it is sometimes associated with apatite and xenotime (Figures 6c and 7a). Some feldspar crystals are altered to sericite, kaolinite, and chlorite due to the effect of hydrothermal fluids, which in turn have caused these alteration products (Figure 5).

## 5. Mineral Chemistry

### 5.1. Major Element Composition

Major element contents of plagioclase, K-feldspar, amphibole, and accessory minerals including magnetite, goethite, ilmenite, titanite, rutile and apatite, along with rare metal-bearing minerals such as monazite, rutile, tantalite, zircon, parisite, and xenotime in the Igla Ahmr granites, were analyzed using an electron probe microanalyzer (EPMA) with wavelength dispersive X-ray spectrometry (JEOL JXA-8600SX) (JEOL Ltd., Tokyo, Japan) housed at Niigata University, Japan (207 analyzed points; Supplementary Table S2). Some elements in rare metal-bearing minerals were confirmed by energy dispersive X-ray spectroscopy (EDS) at Niigata University. Some minerals (biotite and chlorite) were determined using EPMA with wavelength dispersive X-ray spectrometry (JEOL JXA-8230-XM160041-0041) at the Graduate School of Science, Chiba University, Japan. For more information, please check the Supplementary Figure File.

Representative points of both plagioclase (24 points) and alkali feldspars (31 points) in both syenogranites and alkali feldspar granites were analyzed and are listed in Supplementary Table S2. The investigated plagioclase ranges in composition from albite to oligoclase (Figure 8a), with considerable variation in anorthite content (0.17–23.8 mol.%) (Supplementary Table S2). The investigated plagioclase gives  $Ab_{90}An_9Or_1$  as average

compositions (Supplementary Table S2). Otherwise, the K-feldspar plots at orthoclase end-member, with an average composition of  $Ab_4An_0Or_6$  (Supplementary Table S2). The investigated alkali feldspar plots in the microcline–orthoclase–sanidine field (Figure 8b) based on the feldspar classification diagram [34].

Biotite (17 points) in both syenogranites and alkali feldspar granites has an average composition of  $SiO_2$  (36.78 wt.%),  $TiO_2$  (2.94 wt.%),  $Al_2O_3$  (13.10 wt.%),  $FeO^t$  (25.87 wt.%),  $MgO$  (7.19 wt.%), and  $K_2O$  (9.13 wt.%). The analyzed points of biotite plot mainly in the field of primary biotite (Figure 8c) based on the biotite discrimination diagram [35]. Moreover, the biotite in syenogranites has a chemical composition similar to sub-alkaline biotite, whereas biotite data in alkali feldspar granites plot in the calc-alkaline and alkaline/peralkaline biotite field [36] (Figure 8d).

Representative analyses of amphibole (11 points) in syenogranites and alkali feldspar granites are listed in Supplementary Table S2. The analyzed amphibole crystals are primary with high  $TiO_2$  (>0.7 wt.%). According to classification diagram of Leake et al. [37], the analyzed amphiboles are calcic type. They plot in the field of ferroedenite (Figure 8e). The studied magmatic amphiboles have slightly high  $Fe\#$  ( $Fe/(Fe + Mg)$ ) contents with a range from 0.53 to 0.72 (Supplementary Table S2), reflecting the early crystallization of amphibole from granitic parent magmas.

The analyzed chlorite (25 points) has significant  $FeO^t$  (35.36 wt.%, on average),  $Al_2O_3$  (17.51 wt.%), and  $MgO$  (7.46 wt.%) (Supplementary Table S2). This chlorite is secondary in origin and derived from the alteration of biotite (Figure 5). Chlorite is mainly ripidolite, brunsvigite, and diabanite [38] (Figure 8f).

Zircon is found in all granitic phases and stream sediments of the Igla Ahmr area. It shows limited variations in its composition. Zircon contains high  $ZrO_2$  (63.57–66.02 wt.%) and  $SiO_2$  (34.45–35.14 wt.%) in alkali feldspar granites as well as in stream sediments, i.e.,  $ZrO_2$  (64.02–65.60 wt.%) and  $SiO_2$  (33.89–35.15 wt.%) (Supplementary Table S2).

## 5.2. Compositions of Trace Elements

Trace element concentrations of few feldspar and chlorite crystals (Supplementary Table S3) in Igla Ahmr alkali feldspar granites were determined in situ by laser ablation-inductively coupled plasma mass spectrometry (LA-ICP-MS) using a quadrupole ICP-MS (Agilent 7500a) (Agilent Technologies, Inc., Santa Clara, CA, USA) coupled to a 213 nm Nd: YAG laser ablation system (New Wave Research UP213) housed at Niigata University, Japan. For more information about the analytical methods and conditions of LA-ICP-MS, please see the Supplementary Figure File.

Albite and K-feldspar in alkali feldspar granites show very low concentrations of trace and rare earth elements (REEs) with  $\Sigma REEs$  of 0.087 ppm and 0.009 ppm, respectively (Supplementary Table S3). Figure 9a shows that albite and K-feldspar patterns exhibit positive Pb anomaly, according to chondrite (CI)-normalized REEs and primitive mantle (PM)-normalized spider patterns [39]. Chlorite in alkali feldspar granites shows variable concentrations of trace elements with significant amounts of Zn (60 ppm), Li (14.4 ppm), V (9.4 ppm), Ga (6.7 ppm), and Sc (2.8 ppm), and very low contents of REEs ( $\Sigma REEs$ : 0.68 ppm; Supplementary Table S3). The CI-normalized REE patterns of chlorite show negative Eu and Ce anomalies (Figure 9e; [39]). The PM-normalized spider patterns of chlorite exhibit positive anomalies of U, La, Pb, Nd, and Sm, and negative Ba and Eu anomalies (Figure 9f; [39]).

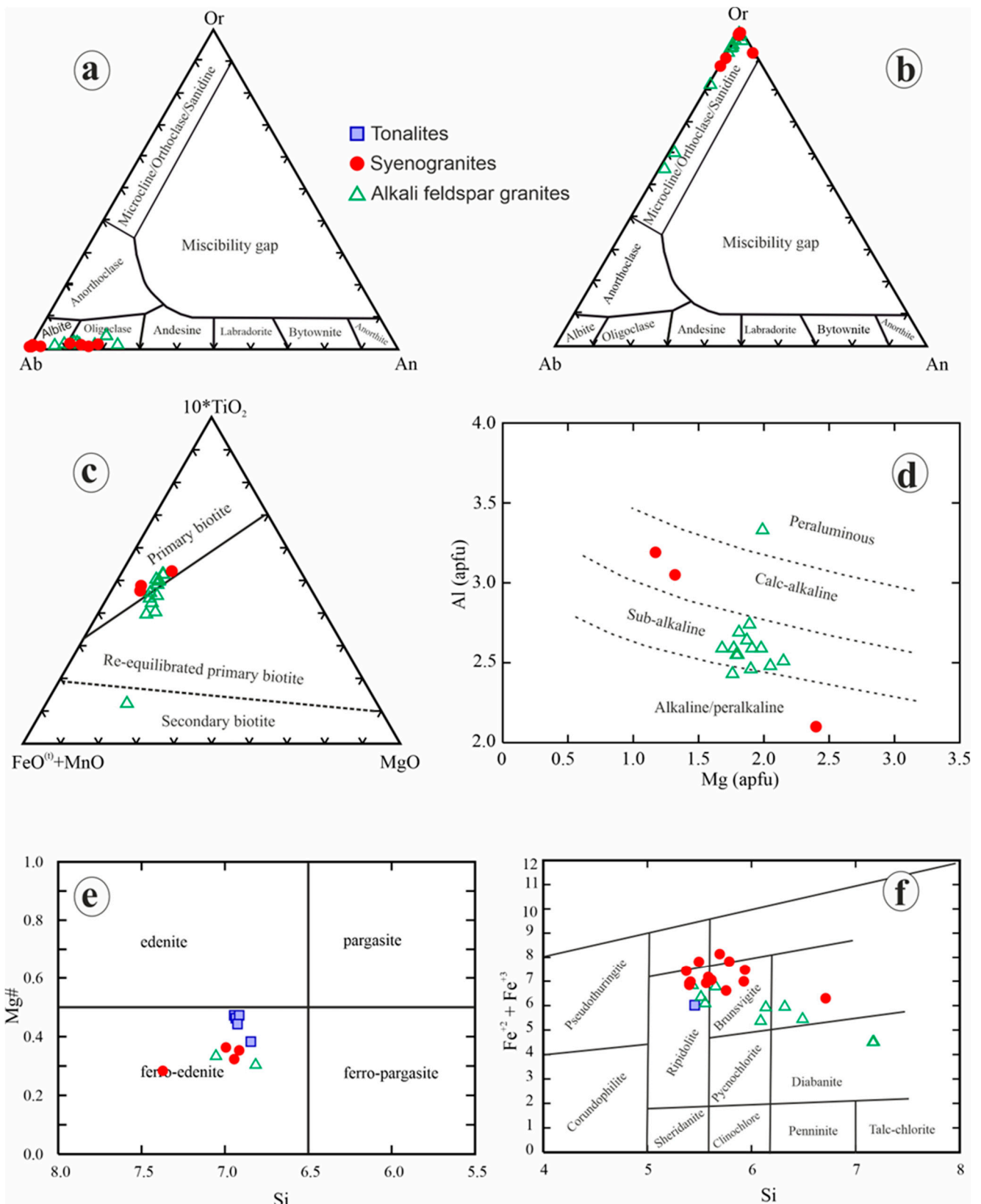


**Figure 8.** Mineral chemistry of the Igla Ahmr granites. (a,b) Feldspar compositions plotted on an albite (Ab)-anorthite (An)-orthoclase (Or) ternary diagram [34]. (c)  $10 * \text{TiO}_2$ -( $\text{FeO}^{\text{I}} + \text{MnO}$ )- $\text{MgO}$  ternary diagram for classification of biotite [35]. (d) Mg versus Al discrimination diagram of analyzed biotites [36]. (e) Si versus Mg# discrimination diagram of amphibole [37]. (f) Si versus ( $\text{Fe}^{2+} + \text{Fe}^{3+}$ ) binary diagram for classification of chlorites [38].

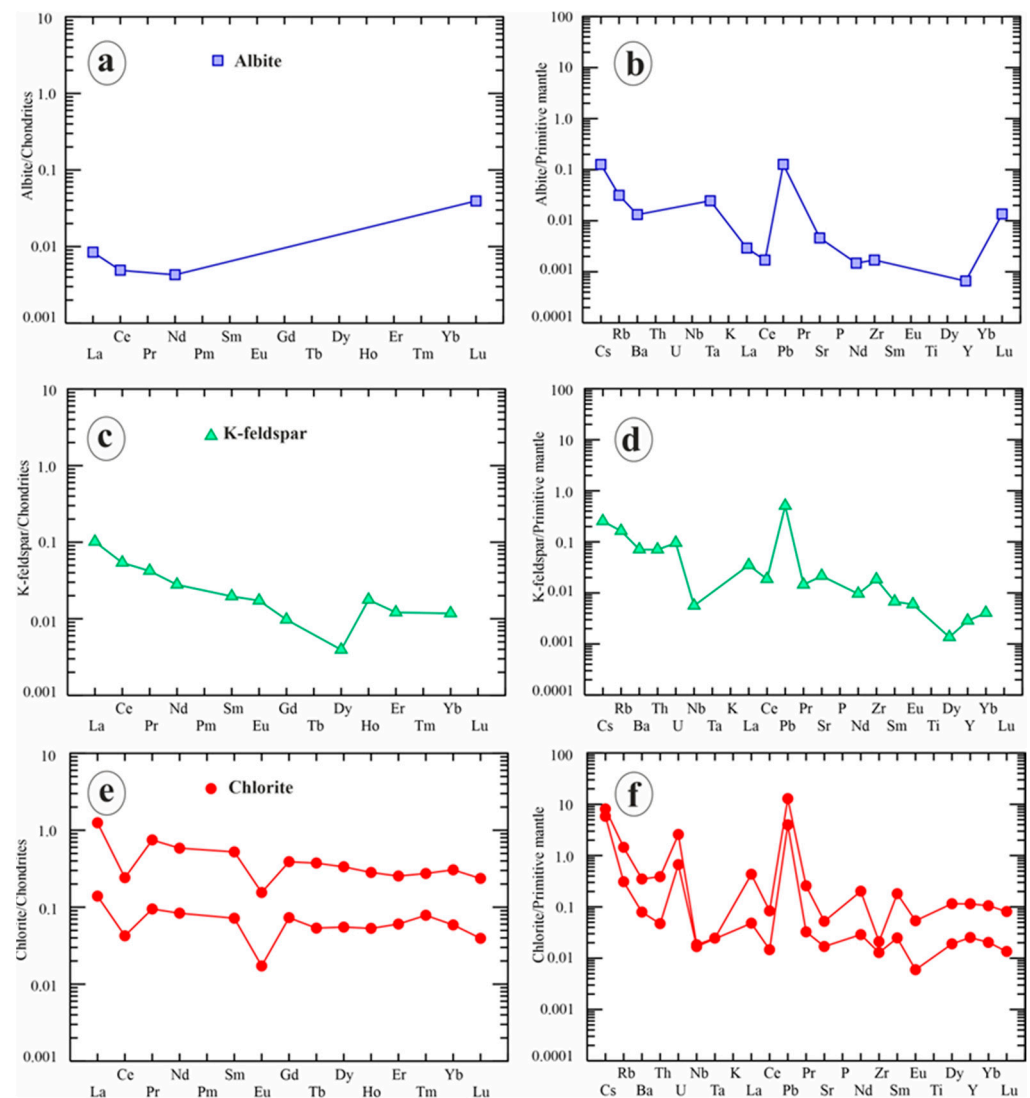


**Figure 9.** In situ analyses of albite, K-feldspar, and chlorite for REEs and trace elements in alkali feldspar granites. (a) Chondrite (CI)-normalized REE patterns of albite. (b) Primitive mantle (PM)-normalized trace element patterns of albite. (c) The CI-normalized REE patterns of K-feldspar. (d) The PM-normalized trace element patterns of K-feldspar. (e) The CI-normalized REE patterns of chlorite. (f) The PM-normalized trace element patterns of chlorite. REE and trace elements are normalized to CI and PM values, respectively, after Sun and McDonough [39].

## 6. Whole-Rock Chemistry

The analyzed granitoid samples have been selected from different varieties based on petrographic description. The Igla Ahmr granitic varieties (19 samples) were selected for major, trace, and REE analyses. XRF and ICP-MS analyses were carried out at the GeoAnalytical Lab, Washington State University (WSU), Pullman, WA, USA. For more details about the XRF and ICP-MS analyses, see the Supplementary Figure File.

The Igla Ahmr syenogranites and alkali feldspar granites are highly evolved with a high silica content (71.46–77.22 wt.%) compared to tonalites ( $\text{SiO}_2 = 65.34$  wt.%) (Supplementary Table S4). All granitic types have high total alkali contents (6.99–8.49 wt.%), except for one sample of alkali feldspar granites, which has a low alkali content (5 wt.%) (Supplementary Table S4). Their average differentiation index is high (D.I. = 95.73), similar to ANS granites [4–7], and their  $\Sigma\text{REE}$  (214 ppm on average) increases with the increase in the D.I. (Supplementary Table S4). The studied granites have slightly high  $\text{Na}_2\text{O}$  (4.33 wt.%, on average) and  $\text{K}_2\text{O}$  (3.43 wt.%), moderate  $\text{Al}_2\text{O}_3$  (12.91 wt.%), but lower  $\text{FeO}^t$  (1.84 wt.%),

CaO (0.76 wt.%) and MgO (0.18 wt.%) as well as TiO<sub>2</sub> (<0.18 wt.%) values than the average composition of the continental crust values ([40]; Supplementary Table S4). The Igla Ahmr granites have relatively low K<sub>2</sub>O/Na<sub>2</sub>O ratios of 0.82 (Supplementary Table S4). Additionally, syenogranites and alkali feldspar granites have low Mg# [ $\text{MgO}/(\text{MgO} + \text{FeO}) \times 100$ ] ratios of 1.95–13.90, but tonalites have high Mg# of 25.69 (Supplementary Table S4). The high Na<sub>2</sub>O content of the Igla Ahmr granites is due to abundant oligoclase (Figure 7a; Supplementary Table S2), implying the change in Ca-rich plagioclase composition by Na-metasomatism, forming dominant Na-rich plagioclase.

The studied granites display enriched REEs ( $\Sigma\text{REEs}$  up to 230 ppm), high field strength elements (HFSEs) as Zr (up to 481.55 ppm) and Nb (up to 14.0 ppm). They are rich in Ba (467.45 ppm on average), Rb (70.54 ppm), Sr (66.96 ppm), Y (48.74 ppm), Sn (12–22 ppm), Ga (15.78 ppm, on average), Th (12.28 ppm), and Nb (8.65 ppm on average), but are low in U (2.48 ppm), Ta (0.67 ppm), and W (0.61–4.57 ppm). The studied granites are peraluminous (molar A/CNK:  $\text{Al}_2\text{O}_3/(\text{CaO} + \text{Na}_2\text{O} + \text{K}_2\text{O}) > 1$ ), except one sample of alkali feldspar granite, which shows metaluminous affinity (Supplementary Table S4). The studied granites are characterized by high LREEs/HREEs fractionation [ $(\text{La}/\text{Yb})_{\text{N}} = 1.88\text{--}6.36$ ] and show a clear tetrad effect of REE patterns ( $\text{TE}_{1-3} = 1.01\text{--}1.09$ ) (Supplementary Table S4). On the R1–R2 classification diagram [41], the Igla Ahmr granites lie mainly in the field of syenogranites and alkali feldspar granites with subordinate tonalite (Figure 10).

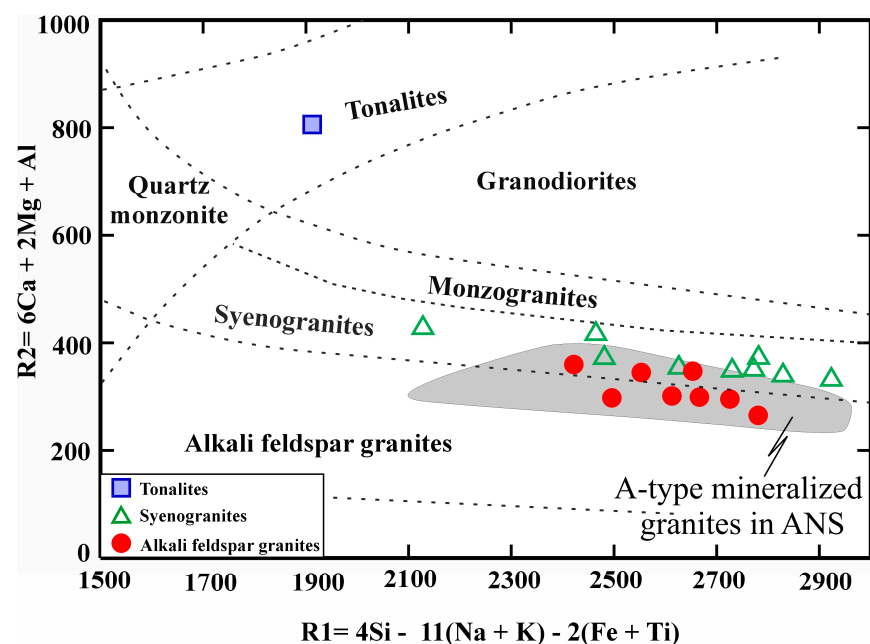


**Figure 10.** R1–R2 classification diagram [41] of the Igla Ahmr granites. All samples are mainly syenogranites and alkali feldspar granites except one sample of tonalites. The field of A-type mineralized granites in the ANS collected from the Umm Naggat, Homrit Waggat, and El-Inegi areas is modeled after Sami et al. [4] and Khedr et al. [7].

The CI-normalized REE patterns [39] of syenogranites and alkali feldspar granites (Figure 11a) display enrichment in light rare earth elements (LREEs) relative to heavy rare earth elements (HREEs) with negative Eu anomalies ( $\text{Eu}/\text{Eu}^* = 0.24\text{--}0.43$ ; Supplementary Table S4), like those of A-type granites in the ANS [4–7]. The negative Eu anomalies are possibly related to feldspar separation from the melt either through crystal fractionation or during partial melting of the feldspar-rich source material. The primitive mantle-normalized trace elements [39] of the Igla Ahmr granites exhibit negative Nb, Ta, P, and Ti anomalies and positive Rb, Th, U, and Pb, similar to A-type granites in the ANS [4,6,7] (Figure 11b).

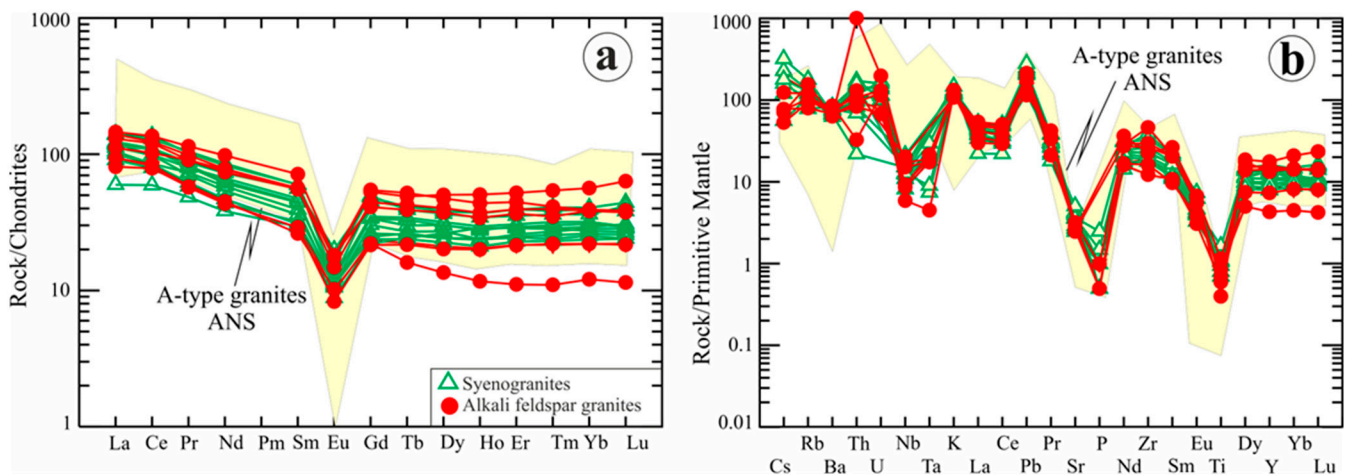


**Figure 11.** Chondrite (CI)-normalized REE patterns of the Igla Ahmr granites. (a) The CI-normalized REE patterns of granites. (b) Primitive mantle (PM)-normalized trace element patterns of syenogranites and alkali feldspar granites. The field of ANS A-type granites is used for comparison [4,6,7]. REE and trace elements of granites are normalized to CI and PM values, respectively, after Sun and McDonough [39].

## 7. Discussion

### 7.1. Mapping of Rare Metal-Bearing Granites Using Machine Learning Algorithms

Localizing geological characteristics associated with the target mineralization through the use of lithological units, different types of alteration, structures, and index minerals is one of the essential steps in mineral exploration [8,33,42–44]. There are some limitations in the prospective modeling in this study due to the lack of information for ore body depth from geophysical surveys. In this study, the machine learning algorithms, which include weighted sum and random forest maps, produce credible predictions with major implications for future research. Chemical analysis, ASTER hydrothermal alteration indices, and line density are the input tools of the deep learning methods, which are used to predict the concentration of rare metals in wide areas to save time and money. We evaluated the high rare metal mineralization in specific regions in the Igla Ahmr area (Figures 2 and 3). The expected concentration of rare metals based on machine learning algorithms was confirmed by the whole-rock analysis of different granitic varieties. This is in agreement with the geochemical data of collected samples from the Igla Ahmr granites, where mineralized granites occur in these high-potential regions (Figures 2 and 3).

The mineral potential map was delineated to translate the concentration of total REEs and associated elements such as Zr, Nb, Ga, Y, Sc, Ta, Mo, U, and Th as well as line density and five alterations indices (Supplementary Figure S2) into mappable exploration criteria for REEs (Figures 2 and 3). This will help our community to explore high contents of rare metals in new areas using the same techniques. The gained information was used to assess the relative weights of each practical feature that was used to examine the model. The findings reveal that the predictive models are most significantly influenced by intrusion-related components acting as proxies for the source process. With the superior values for sensitivity, negative predictive value, and accuracy, the performance assessment reveals that the random forest model has the highest predictive accuracy in both the training and test datasets (Figures 2 and 3; Supplementary Figure S2). This is consistent with Pradhan et al. [23] and Sun et al. [45] who stated that the random forest is the best machine learning method, and yielded a more accurate prediction than the weighted sum method.

### 7.2. $P$ - $T$ and $f_{O_2}$ Conditions of Granite Crystallization

The high Zr concentration (up to 482 ppm) in the Igla Ahmr granites in addition to zircon morphology and chemistry is relatively similar to that of the ANS granites [4,6,7].

The Zr value in syenogranites and alkali feldspar granites ranges from 184 to 342 ppm and 127 to 482 ppm, respectively (Supplementary Table S4). On the other hand, tonalites have a Zr content of 317 ppm (Supplementary Table S4). Zircon saturation temperature ( $T_{Zr}$ ) was estimated based on the whole-rock chemistry of the Igla Ahmr granites by using the equation after Boehnke et al. [46]. Consequently, this  $T_{Zr}$  for tonalites, syenogranites, and alkali feldspar granites is 763 °C, 807 °C, and 775 °C on average, respectively (Supplementary Table S4). There is slightly increasing of temperatures from tonalites to alkali feldspar granites due to the fractionation of magma to crystallize several phases or several magmatic impulses. The calculated  $T_{Zr}$  of the Igla Ahmr granites is similar to that (717 °C to 820 °C) of A-type granites in the ANS [7].

In this study, pressure can be estimated based on whole-rock chemistry (Supplementary Tables S2 and S4). A mathematical method after Yang [47] was used for pressure calculation [ $P = -0.2426 \times (Qtz)^3 + 26.392 \times (Qtz)^2 - 980.74 \times (Qtz) + 12563$ ], where Qtz is normative quartz and P is pressure in MPa. The average calculated pressure of syenogranites is 1.73 kbar at a depth of nearly 5.7 km, and alkali feldspar granites is 1.42 kbar at a depth ~4.7 km (Supplementary Table S4), suggesting that both granite types crystallized in the upper crust. In addition, the Qz–Ab–Or diagram (Figure 14f) shows that the Igla Ahmr syenogranites and alkali feldspar granites plot close to the minimum melt composition at ~2 kbar to ~4 kbar, except for two samples that plotted between 6 and 8 kbar with excess H<sub>2</sub>O rich fluid including 0.5% to 4% F [48]. This indicates a maximum pressure of up to 4 kbar at a depth of up to 13.5 Km in the upper crust. On the other hand, tonalites plot near the albite apex, implying the role of hydrothermal metasomatism in the generation of tonalites.

The oxygen fugacity ( $f_{O_2}$ ) of the Igla Ahmr granites could be calculated from the equilibrium expression equation [ $\log f_{O_2} = -30930/T + 14.98 + 0.142(P - 1)/T$ ; [49], where T is temperature (in Kelvin), and P is pressure (bars). By using the previous zircon saturation temperature ( $T_{Zr}$ ) and pressure based on whole-rock chemistry, the calculated oxygen fugacity ( $\log f_{O_2}$ ) of tonalites is  $-14.50$ , which was compared with the commonly used oxygen fugacity buffer, e.g., the fayalite-magnetite-quartz (FMQ) buffer as  $+1.67$ . The  $\log f_{O_2}$  of syenogranites ranges from  $-13.0$  to  $-14.28$  (FMQ:  $+3.17$  to  $+1.89$ ) and alkali feldspar granites have  $\log f_{O_2}$  values in the range  $-10.9$  to  $-15.2$  (FMQ:  $+5.27$  to  $+0.97$ ) (Supplementary Table S4); this suggests that the Igla Ahmr granites originated in relatively oxidized conditions (e.g., [6,7]).

### 7.3. Petrogenesis of Igla Ahmr Granites

#### 7.3.1. Magma Type and Tectonic Setting

The Igla Ahmr granites are highly fractionated ( $SiO_2 > 68$  wt%) with a slightly peraluminous character ( $A/CNK > 1$ ) (Supplementary Table S4). Based on a discrimination diagram of Sylvester [50], the syenogranites and alkali feldspar granites lie in the highly fractionated calc-alkaline field (Figure 12a). Moreover, they are similar to ferroan A-type granites, except tonalites lie in the field of magnesian granites [51] (Figure 12b). Syenogranites show alkali to calc-alkalic affinities ([51]; Figure 12c), whereas tonalites and alkali feldspar granites display calc-alkalic affinity. The analyzed syenogranites and alkali feldspar granites show a peraluminous affinity (molar  $A/CNK: (Al_2O_3/CaO + Na_2O + K_2O) = 1-1.79$ ) (Figure 12d). This is consistent with their high normative corundum contents (up to 6.0 wt.%; Supplementary Table S4), and Al-rich phases such as primary muscovite [8], and biotite (Figure 7c,d). On the other side, tonalites show a metaluminous affinity (Figure 12d).

The Igla Ahmr granites show characteristics of A<sub>2</sub>-type granite (except tonalites of I-type), originated in the post-collisional setting (Figures 12 and 13). On the other hand, the Igla Ahmr tonalites exhibit features of I-type granites such as high  $Al_2O_3$  (16.41 wt.%),  $FeO^t$  (4.0 wt.%) and  $MgO$  (1.39 wt.%) contents (Figure 5b; Supplementary Table S2), but are low in silica content ( $SiO_2 = 65.34$  wt.%),  $K_2O/Na_2O$  (0.18 wt.%) and  $A/CNK$  (0.93), in addition to having a metaluminous character and an absence of normative corundum

(Supplementary Table S4) [6,18]. They plot in the I-type granite (Figure 12e), like phase I granite (Figure 13d).

The investigated syenogranites and alkali feldspar granites are slightly peraluminous A-type granites. The investigated A-type granites display chemical characteristics such as high SiO<sub>2</sub> (71.46–77.22 wt.%), high alkali (up to 9 wt.%), Zr (up to 482 ppm), FeO<sup>t</sup> / (FeO<sup>t</sup> + MgO) ratios > 0.86, A/CNK ratios > 1, ΣREEs (102–230 ppm), and high Al<sub>2</sub>O<sub>3</sub> + CaO < 15 wt.%, but are low in CaO and MgO contents (Supplementary Table S4). Consequently, these granites mainly exhibit an affinity of A-type granites (e.g., [3–7,17,51,52]). These granites belong to the low-P subtype of rare metal granites, characterized by high silica contents, mainly (SiO<sub>2</sub> > 73 wt.%), (Al<sub>2</sub>O<sub>3</sub> < 14.5 wt.%) and (P<sub>2</sub>O<sub>5</sub> < 0.1 wt.%), similar to Deleihimmi granites in the CED of Egypt [53] (Supplementary Table S4).

In the Zr vs. 10<sup>4</sup> × Ga/Al diagram [17], tonalites and a few syenogranite samples plot in the I-type granite field, while all alkali feldspar granites and other syenogranites plot in the A-type granite field (Figure 12e). Stern and Ali [29] identified three primary granitic magmatism periods in the CED, including I-type granitoids (710–630 Ma), A-type granites (620–580 Ma), and minor Cadomian (550–540 Ma) rock types. The Igla Ahmr granites are older phases of the transitional between I-type and A-type mineralized granites in the Eastern Desert of Egypt, formed at 691.7–678.9 Ma with δ<sup>18</sup>O<sub>V-SMOW c.</sub> 5.95‰ [9]. Therefore, some of our syenogranites lie in both fields of I- and A-type granites (Figure 12e). Additionally, the studied alkali feldspar granites plot in the A<sub>2</sub> field (Figure 12f; [52]) and are considered A<sub>2</sub>-type granites formed in a post-collisional setting (e.g., [4–7]). Finally, the Igla Ahmr A-type granites with subordinate I-type (tonalites) have high ΣLREEs relative to ΣHREEs (Figure 11a). They are depleted in Sr, P, and Ti due to the fractionation of plagioclase and apatite during the formation of early-formed I-type granites (Figure 11b; Supplementary Table S4).

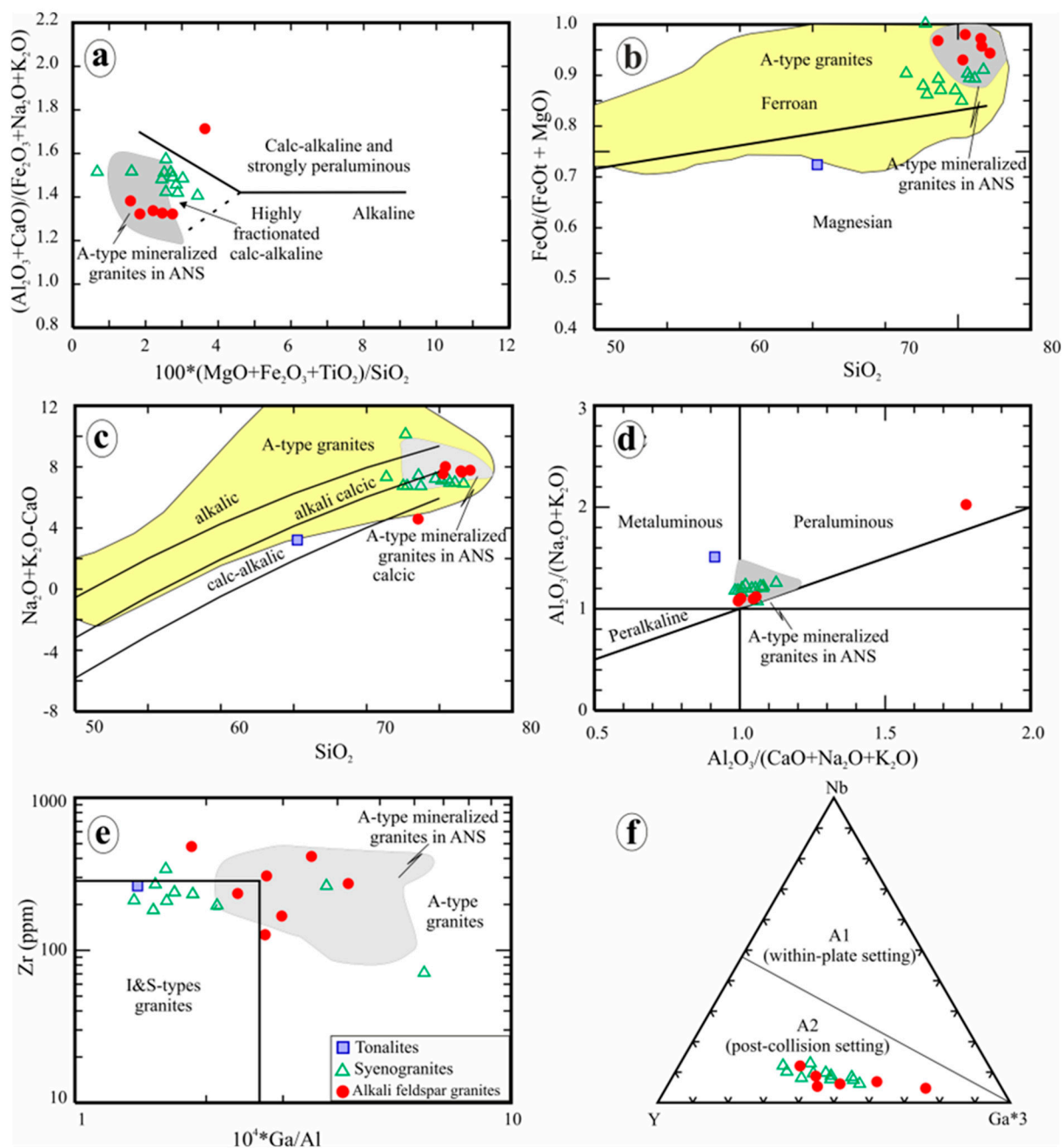


**Figure 12.** Magma type of the Igla Ahmr granites. (a) Discrimination diagram using  $100 \cdot (\text{MgO} + \text{FeO}^t + \text{TiO}_2) / \text{SiO}_2$  vs. molar  $(\text{Al}_2\text{O}_3 + \text{CaO}) / (\text{FeO} + \text{Na}_2\text{O} + \text{K}_2\text{O})$  to differentiate between calc-alkaline, highly-fractionated calc-alkaline, and alkaline granites [50]. (b) Chemical classification diagrams using  $\text{SiO}_2$  vs.  $(\text{FeOt} / (\text{FeO}^t + \text{MgO}))$  of Frost [51]. (c) Chemical classification diagram using  $\text{SiO}_2$  vs.  $(\text{Na}_2\text{O} + \text{K}_2\text{O}) - \text{CaO}$  [51]. The A-type granite field is modeled after Whalen et al. [17]. (d) Molar  $\text{Al}_2\text{O}_3 / (\text{Na}_2\text{O} + \text{K}_2\text{O})$  vs.  $\text{Al}_2\text{O}_3 / (\text{CaO} + \text{Na}_2\text{O} + \text{K}_2\text{O})$  for the studied granites [54]. (e)  $10^4 \cdot \text{Ga} / \text{Al}$  against Zr for distinguishing between I, S, M and A-type granites [54]. (f) The discrimination diagram of Nb-Y-Ga/3 showing subdivision of A-type granites into A<sub>1</sub> and A<sub>2</sub> sub-types, where A<sub>1</sub> and A<sub>2</sub> have element ratios similar to those observed for oceanic-island basalts and continental crust, respectively [52]. The field of A-type mineralized granites in the ANS collected from Umm Naggat, Homrit Waggat, El-Inegi, Abu Dabbab, Nuweiba, Mueilha, and Abu Diab areas is modeled after Sami et al. [4]; Azer et al. [5]; Seddik et al. [11]; Moussa et al. [55]; Khedr et al. [7]; and Abuamarah et al. [56].

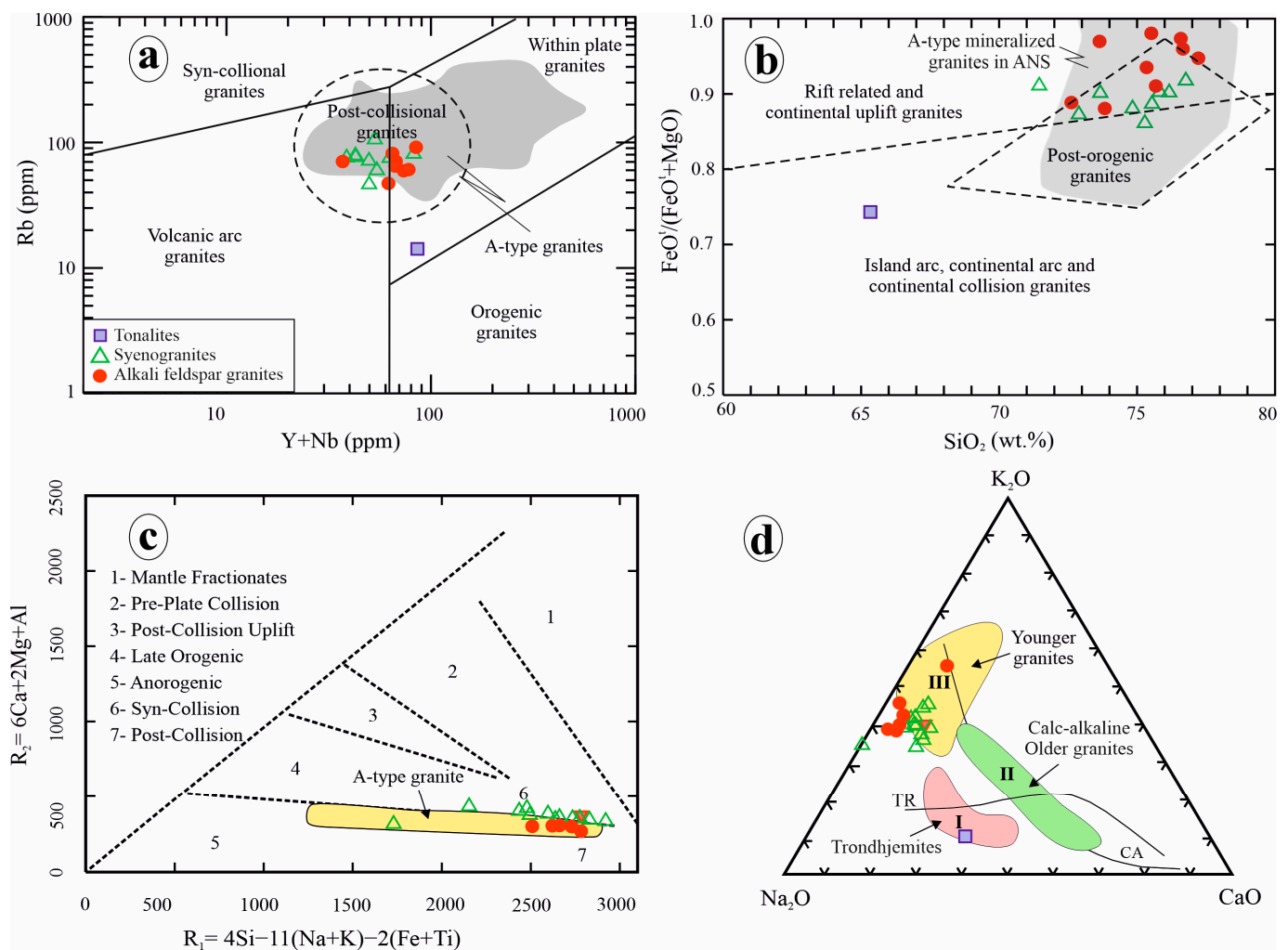


**Figure 13.** Tectonic setting of the Igla Ahmr granites. (a) Y + Nb vs. Rb tectonic discrimination diagram [2]. Post-collisional granites are after Pearce [57]. (b) SiO<sub>2</sub> versus FeO<sup>t</sup>/(FeO<sup>t</sup> + MgO) tectonic discrimination of Maniar and Piccoli [54]. (c) R<sub>1</sub>-R<sub>2</sub> multi-cationic diagram [58]. (d) Na<sub>2</sub>O-K<sub>2</sub>O-CaO ternary diagram of Egyptian granitoids [4,6,7,59]. Field of trondhjemites and calc-alkaline are after Barker and Arth [60], while the field of A-type mineralized granites in the ANS as in Figure 12.

On the binary Y + Nb-Rb diagram after Pearce et al. [2], syenogranites and alkali feldspar granites plot in the field of post-collisional granites, while tonalites lie in the space close to this field (Figure 13a). There are systematic correlations between major elements such as Si, Fe, and Mg versus Zr (immobile element) in the Igla Ahmr granites (Supplementary Figure S3g,h; S4a and S5d), suggesting these major elements are immobile during post-magmatic alteration and used in tectonic diagrams. Based on the SiO<sub>2</sub> versus FeO<sup>t</sup>/FeO<sup>t</sup> + MgO tectonic discrimination diagram, tonalites plot in the field containing island-arc, continental-arc, and continental collision granitoids (Figure 13b; [54]), reflecting their origin during the syn- to post-collisional stage. These tonalites (I-type) have low A/CNK = 0.93 and are similar to island-arc or continental arc granitoids that evolve in subduction zones [56]. On the other hand, the studied A-type granites are classified as post-orogenic granites based on SiO<sub>2</sub> versus FeO<sup>t</sup>/FeO<sup>t</sup> + MgO diagram (Figure 13b; [54]). These I-type and A-type granites plot in the space of both syn-collision and post-collision, respectively, based on R<sub>1</sub>-R<sub>2</sub> ratios (Figure 13c; [58]), suggesting their transitional origin between I-type and A-type and their tectonic setting transition from syn-collision to post-collision. The chemistry of the biotite crystal supports the results obtained from whole-rock

geochemistry (Figure 8c,d), where biotite composition is mostly intermediate between calc-alkaline and alkaline suites [32] that are a characteristic feature of post-collisional intrusions in the ANS [5,53]. The studied A-type granites are similar to the Egyptian younger granites (Figure 13d), while tonalites plot in the field of trondhjemites. The REE patterns of the Igla Ahmr syenogranites and alkali feldspar granites fill the space of post-collisional A-type granites in the ANS (Figure 11a; [4,6,7]). In summary, the Igla Ahmr I-type tonalites crystallized from peraluminous magmas in the arc-related setting during the arc-arc collision, while syenogranites and alkali feldspar granites are mainly A-type granites that originated in the post-collision setting.

### 7.3.2. Petrogenesis Model of Rare Metal-Bearing Granites

There are debates regarding the origin of the Igla Ahmr I- and A-type granites and if their origin and parent melts from the melting of the crustal source rocks or from mantle-derived magmas that are contaminated with crustal sources during assimilation or anatexis [8,9]. In order to answer, we will discuss in the following lines the difference between granites derived from crustal and mantle source materials using some trace elements. We selected some trace elements of granitic rock, which were not affected by metasomatism and hydrothermal alteration. For instance, the systematic relationships between immobile Zr versus Nb/Ta and Y/Nb reflect immobility of Nb, Ta and Y in the Igla Ahmr granites and they can be utilized to determine their origin (Supplementary Figures S4f and S5b–f). The mantle sources have Y/Nb ratios of <1.2, while the Y/Nb ratio for materials of a crustal origin is more than 1.2 [52]. The Igla Ahmr I- and A-type granites have Y/Nb values (3.93–6.88), reflecting their crystallization from melts of crustal materials (Supplementary Table S4). In addition, the mantle-derived melts have a higher Nb/Ta ratio (>17.5) than the typical continental crust value of less than 17 [40,61]. The Nb/Ta values (7.53–15.44) of the Igla Ahmr A-type granites suggest their crystallization from crustal source magmas, but these values are also close to the range of mantle-derived melts (Supplementary Table S4), reflecting considerable contribution from the mantle source. This is in agreement with the isotopic data of the Igla Ahmr granites, which have positive initial  $\epsilon_{\text{Nd}}$  values (+3.3 to +6.9) with  $\delta^{18}\text{O}_{\text{V-SMOW c.}}$  5.95‰, typical for mantle and juvenile crust [9]. Therefore, the Igla Ahmr granites possibly crystallized mainly from partial melting of crustal source (possibly tonalite) rocks that were intermixed with some parts of mantle-derived melts.

Assimilation–fractional crystallization (AFC) is the most likely differentiation mechanism [62] for the examined granitoids (Figure 14a,b). During ascent and storage of the parent magmas in higher crustal levels, these mantle-derived magmas concurrently absorb and assimilate crustal rocks during assimilation processes and the resultant mixed magmas were evolved during fractional processes and crystallization of the first-stage granite. The relative rate of assimilation and crystallization is an important factor controlling the parent magma compositions and the compositions of the primitive magma and assimilated crustal materials. This is further supported by the plotting of the investigated tonalites on the ternary discrimination source diagram [63], which suggests that the tonalites were derived from a low-K mafic source (Figure 14c). According to petrography, the frequent occurrence of oscillatory-zoned plagioclase (Figure 5a) in the investigated tonalites may point to a specific type of the open-system magmatic process [3].

Using whole-rock data, we attempted to estimate the contribution of crust versus mantle in magma genesis of the Igla Ahmr granites using the Rb versus K/Rb diagram [64] and Th/Nb ratios versus Zr contents (Figure 14a,b). Based on these diagrams, the Igla Ahmr I- and A-type granites take assimilation and fractional crystallization trends (Figure 14a,b). The Y/Nb (~3.93–6.88) values of the Igla Ahmr granites are primarily consistent with those of granite that mainly originated from a crustal source (like tonalite melts) (Supplementary Table S4) [6,7,40,52,65]. The studied granites are higher in Nb (3.91–13.45 ppm) than Ta (0.34–1.2 ppm) contents (Supplementary Table S4) with high Nb/Ta ratio, implying crustal sources [66]. On the  $\text{TiO}_2$  versus  $\text{Al}_2\text{O}_3/\text{TiO}_2$  diagram, the curved trend is typical of magmatic

differentiation of Garcia et al. [67] and compatible with the fractional crystallization model (Figure 14e) [53].

From aforementioned results, we found that tonalites are similar to I-type granites and derived from mantle-derived magmas that are contaminated by crustal materials during assimilation. Therefore, we cannot exclude the role of mantle-derived melts in the formation of the Igla Ahmr I-type granites (metaluminous) by significantly fractional crystallization. But the Igla Ahmr A-type granites show the peraluminous character, suggesting that their parent melts have been produced by partial melting of a juvenile crustal source (possibly tonalite), followed by fractional crystallization (Figures 12c, 14 and 15).

It is well known that tonalites (source of A-type magma) crystallized from the partial melting of intermediate and mafic crustal sources above a subduction zone [3,12,68] due to the increasing of the geotherm [3,7,69]. Based on diagrams of granite parent sources [63], the Igla Ahmr A-type granites mainly plot in the field of tonalites (Figure 14c), implying that tonalites could provide an appropriate protolith for the investigated A-type granites that follow the assimilation–fractional crystallization trend [70] (Figure 14a,b). Therefore, the studied tonalites (Figure 14c) may be the primitive source of the Igla Ahmr granites (Figure 14d) (e.g., [5,7,12]). This is consistent with Patiño Douce [71], who stated that the calc-alkaline tonalite (0.4 Gpa) source was considered the primary melt source of A-type granites.

High K<sub>2</sub>O contents of the studied granites (up to 4.11 wt.%; Supplementary Table S4) are possibly related to K-metasomatism along shear zones of NW–SE and N–S trends (Figure 1b). Syenogranites resemble alkali feldspar granites in both texture and chemical composition (Figure 5c–i; Supplementary Table S4), suggesting that they possibly originated from the same parent source such as a partially melted calc-alkaline I-type tonalite source, where the latter is more evolved by fractional crystallization (Figure 14a,b) [5,7,12]. This is in agreement with major, trace, and REE patterns of syenogranites and alkali feldspar granites, which are nearly the same without gaps in their concentrations (Supplementary Figure S3). The residual melts/fluids of a partially melted tonalite source have been enriched in alkalis, silica, water, and rare metals as a result of the crystallization of syenogranites and alkali feldspar granites. These late melts/fluids migrated from the depth to upward, and created fractures that extended into the surrounding rocks and produced greisen, pegmatites, and quartz veins (Figure 4d) (e.g., [5,7,11,12]). The negative P and Ti anomalies in the spider diagram (Figure 11b) reflect minor fractionation of apatite and Fe-Ti oxide, respectively [53]. In summary, the Igla Ahmr A-type peraluminous granites crystallized from primary magmas generated by partial melting of highly fractionated I-type tonalites, followed by extensive fractional crystallization and fluid interaction, while the studied tonalites resemble I-type granites and crystallized from mantle-derived magmas that were contaminated by crustal materials during assimilation.

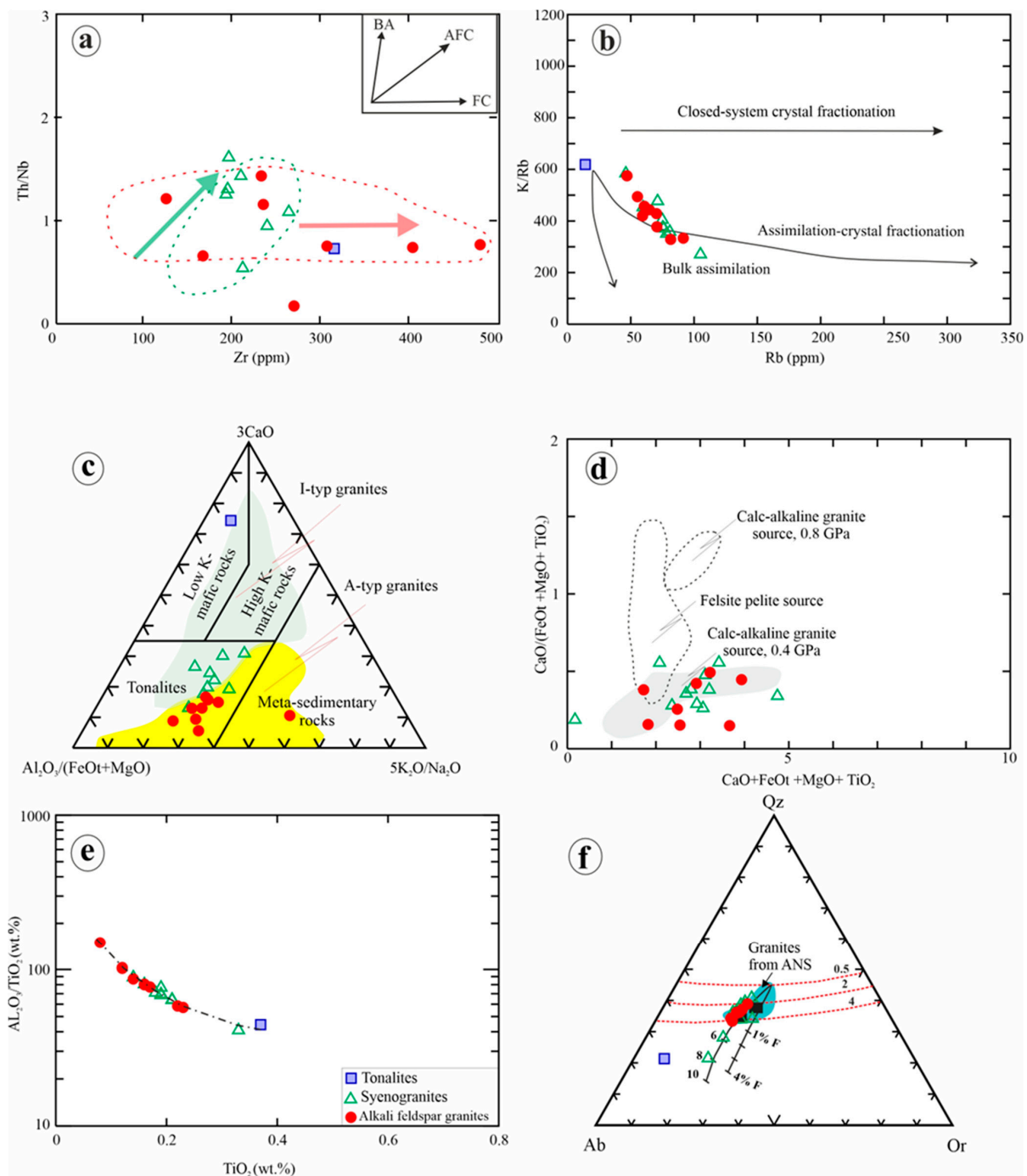


**Figure 14.** Whole-rock compositions of the Igla Ahmr granites showing their origin and thermometry. (a) Zr vs. Th/Nb variation diagrams displaying fractional crystallization (FC), assimilation–fractional crystallization (AFC), and bulk assimilation (BA) trends [70]. (b) The Rb vs. K/Rb diagram for assimilation–crystal fractionation [64]. (c) Petrogenetic discrimination of  $Al_2O_3/(FeOt + MgO)-3CaO-5(K_2O/Na_2O)$  ternary diagram for the studied A-type granites [62]. The fields of A-type and I-type granites in the ANS are adopted from Robinson et al. [72]. (d) Compositions of the Igla Ahmr A-type granites compared to melts produced by experiment of the dehydrated melts of various lithologies [71]. (e)  $TiO_2$  versus  $Al_2O_3/TiO_2$  (wt.%) diagram of the Igla Ahmr granitoids, showing a curvilinear trend of magmatic differentiation (f) Qz–Ab–Or normative compositions for granite thermometry. Dashed lines display quartz-alkali feldspar cotectic limit and trace of water saturated minimum melt compositions at range of pressure from 0.5 to 10 kbar [73]. The trace of minimum melt compositions at 1 kbar with excess  $H_2O$  and increasing fluorine (F, up to 4 wt. %) delineated by solid lines [48].

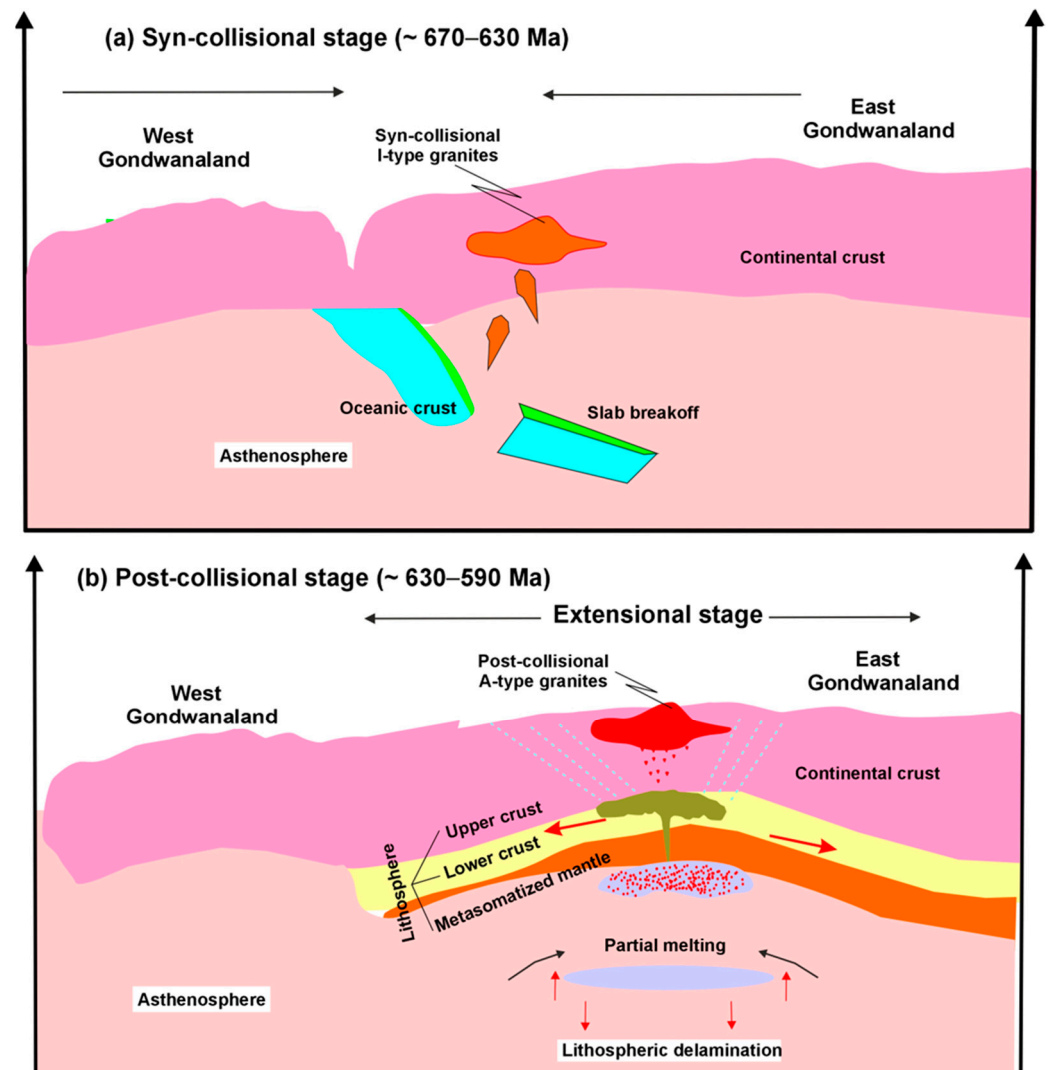


**Figure 15.** The tectono-magmatic evolution of the Igla Ahmr granites. (a) Syn-collision I-type and (b) post-collision A-type granites, showing lithospheric delamination, partial melting of lower crust and formation of A-type granites in the upper crust [5,7,11,74]. Crust and mantle thicknesses are not to scale.

### 7.3.3. Geodynamic Evolution and Development of the CED Juvenile Crust

The Igla Ahmr granites are part of the CED of Egypt, which is part of the ANS. The Neoproterozoic tectonic and geodynamic processes led to the development of the ANS juvenile crust including the collision of East and West Gondwana, post-collisional expansion, and stabilization of the ANS crust [75,76]. The post-collisional granitoids are thought to have formed from melting of crustal rocks following the delamination of the lithospheric root. The role of lithospheric delamination processes in generation of calc-alkaline magmas has also been explained the tectonic of several orogenic zones around the world [4–7,77,78]. The highly fractionated granitoids that evolved in the northern ANS have been interpreted as evidence of a change from collisional to extensional tectonics, making them geodynamically and economically significant [53].

The geodynamic model of the Igla Ahmr granites is shown in Figure 15. The Igla Ahmr tonalites are old granitic phases in the studied area, and show characteristic features of I-Type (Figures 12e, 13b and 14c); these tonalites originated from mantle-derived melts and contaminated with crustal materials (~670–630 Ma; [79]) during the syn-collisional stage (Figure 15a). Then, there is a transitional stage and a change in the tectonic style from

the compressional setting and formation of syn-collisional granites (e.g., I-type tonalites, Figure 4a,b) to the extensional setting and formation of post-collisional granites (e.g., A-type syenogranites and alkali feldspar granites, Figure 4c–f). According to Melcher et al. [80], the Abu Dabbab, Nuweibi, and Igla Ahmr granites are significantly older (616–685 Ma), using the U–Pb age estimates for cassiterite. This fact was recently confirmed by Stern et al. [9], who stated that the Igla Ahmr granites are older phases of the transitional between I-type and A-type mineralized granites in the CED of Egypt, formed at 691.7–678.9 Ma with  $\delta^{18}\text{O}_{\text{V-SMOW c. } 5.95\%}$ . These granites are considered the older phase of rare metal-bearing granites in the Eastern Desert of Egypt [9], and represent the first stage of the transition from syn-collision to post-collisional tectonic settings (Figure 15). During the transition from the compressional to extensional setting (690–590 Ma), the mantle-derived magmas cause extensively partial melting of lower-crustal materials during the starting of lithosphere delamination [77,78], yielding tonalitic parental magmas that crystallized as Igla Ahmr tonalites. During the extensional stage, shearing and extension allowed the fault planes to go to deeper depths, which led to the development of shear zones such the NW–SE Najd shear zones (620–540 Ma; [72]) conjugated with N–S faults (Figure 1b). These faults and shear zones were formed as an effective conduit for asthenosphere-derived melts, volatiles, and fluids, which upward migrated and transferred heat to the shallow crustal level. These fluids generated from magmatic sources are considered the main factor controlling granitic metasomatism and the formation of rare metal-bearing granites, as well as the formation of hydrothermal alteration zones (Figures 4–7) [8].

In order to form parental magmas of the A-type granite, the volatiles/fluids-rich mantle magma migrated upward through the faults/shear zones to a shallower crustal level and accelerated the partial melting of the pre-existing calc-alkaline tonalites in the lower crust (Figure 15). This is inconsistent with the partial melting of tonalitic to granodiorite source rocks to generate A-type granitic parental magmas (e.g., [4–7,19,74,81,82]). These parental magmas exhibit characteristics of A-type granitic magmas, including peraluminous magmatic affinity, higher values of Zr (316 ppm),  $\Sigma\text{REEs}$  (179.51 ppm), and Nb (11.1 ppm) as well as being richer in  $\text{SiO}_2$  and alkalis (Figures 12 and 13; Supplementary Table S3). They crystallized as two granitic phases such as syenogranites and alkali feldspar granites, respectively, by fractional crystallization (Figure 14a,b).

In summary, at the early phase of the post-collisional stage, the magma resulting from upwelling of the hot asthenosphere during lithosphere delamination assimilated huge parts of pre-existing tonalites [6]. The resultant magma includes the addition of mantle materials after partial melting of pre-existing tonalites. During the magmatic process, the magma suffered from fractional crystallization and yielded syenogranites (Figures 14a–c and 15). After that, the more evolved magma was enriched in magmatic-derived fluids generated during the fractionation of peraluminous magmas and crystallized as alkali feldspar granites in the late stage (Figure 15).

#### 7.4. Origin of Rare Metals and Specific Distribution of Rare Metal-Bearing Granites

Several studies have examined the genesis of rare metals (Figure 7; Supplementary Table S2) in the ANS, and three hypotheses include: (1) metasomatic origin (e.g., [83,84]), (2) magmatic origin (e.g., [16,51]), and (3) both magmatic and metasomatic origins (the hybrid origin) ([7,8,11,13,85]). The Igla Ahmr rare metal-bearing granites are mainly magmatic in origin, even with the involvement of subsequent metasomatic processes and formation of some rare metals (e.g., [8]). There are several lines of evidence of the magmatic origin, including (1) the existence of primary feldspars, biotite, zircon, Fe–Ti-oxides in the form of euhedral to subhedral crystals, showing triple junction boundary (Figures 4–7; [7,8]); (2) the whole-rock major, trace, and REE contents showing continuous compositional trends (Supplementary Figures S3–S5; [7]); (3) increasing REE concentrations from syenogranites (102–213 ppm) to the late stage alkali feldspar granites (112–230 ppm) (Supplementary Table S4; [7,85]); (4) the positive correlations of Zr vs. Hf, Nb vs. Ta, and Y vs. Ho (Supplementary Figure S5) suggesting magmatic enrichment of these elements [7,85]; (5) the curved trend of magmatic

differentiation of  $\text{TiO}_2$  versus  $\text{Al}_2\text{O}_3/\text{TiO}_2$  (Figure 14e), reflecting the effect of fractional crystallization after partial melting of lower crust as proposed scenario for the origin of the Igla Ahmr granites (e.g., [53]); (6) the pronounced tetrad effect ( $\text{TE}_{1,3} = 1.08$  and  $1.09$ ) of the Igla Ahmr granites, indicating fractional crystallization at the magmatic stage (Supplementary Table S4; [53]); and (7) the Igla Ahmr granites showing the same chondrite-normalized REE patterns as those of magmatic granites in the ANS (Figure 11).

On the other hand, the action of later metasomatic processes and hydrothermal alteration of some granitic zones can be observed by the following evidence: (1) the formation of thin hydrothermal alteration zones (Figures 4–7) of Igla Ahmr granites; (2) the Igla Ahmr granites being affected by hydrothermal fluids, forming different alteration mineral zones such as sericitization, carbonatization, kaolinitization, and chloritization that were outlined by ASTER indices [8]; (3) the alteration of syenogranite to form kaolinitic alteration zones (Figure 4f); (4) an abundance of silicification (Figure 4d) considered important evidence of hydrothermal metasomatism in syenogranites [8]; (5) alteration of biotite to chlorite (Figure 5); (6) alteration of plagioclase to kaolinite and sericite as evidence of hydrothermal metasomatism (Figure 5e); (7) syenogranites and alkali feldspar granites including high  $\text{Na}_2\text{O}$  contents (up to 5.23 wt.%) due to abundant oligoclase (Figure 8a; Supplementary Table S2) and Na-metasomatism (Supplementary Table S4; [6,7]); and (8) the Igla Ahmr granites having a variety of metasomatic textures and alteration zones, including myrmekitic and micrographic textures, sericitization, chloritization, carbonatization, muscovitization, albitization, kaolinitization, and silicification, based on field observation, petrography, and ASTER mineral indices [8].

Rare metals in the Igla Ahmr pluton are mainly concentrated in the alkali feldspar granites and syenogranites. They crystallized in two stages. The early stage of magmatic origin minerals includes zircon, titanite, apatite and rutile (Figure 7a; Supplementary Table S2). The late stage involves the growth newly mineral phases and partial replacement of the magmatic mineral phases such secondary zircon (metamict type) and xenotime (Figure 7c; Supplementary Table S2). Therefore, the origin of rare metals (hybrid origin [7]) is both magmatic (such as zircon, titanite, and rutile) and hydrothermal (such as allanite, xenotime, parisite). There are several pieces of evidence based on crystal morphology (Figures 6 and 7), texture (Figures 6 and 7), and chemistry (Supplementary Table S4) to support this assumption.

Zircon is the primary accessory mineral in the Igla Ahmr granites and is found as a primary magmatic phase with high  $\text{ZrO}_2$  contents (63.57–66.0 wt.%) (Figures 5–7; Supplementary Table S2). The colorless euhedral prismatic crystals of zircon show oscillatory zoning, and are free from inclusions, suggesting their magmatic origin (Figures 5–7). On the other hand, rare metamict zircon crystals with dark color can be found in the Igla Ahmr granites and they host few U, Th, and Hf contents. Rutile is found as subhedral prismatic crystals between silicate minerals or within K-feldspar crystals (Figure 7b), reflecting a magmatic origin. It has high  $\text{TiO}_2$  (95.51 to 97.64 wt.%) and low  $\text{Nb}_2\text{O}_5$  (0.93 wt.%) contents in alkali feldspar granites (Supplementary Table S2).

Xenotime ( $\text{YPO}_4$ ) has been recorded in the Igla Ahmr granites; it hosts high contents of HREE (Figure 7c; Supplementary Table S2). It exists in the rim of Fe-Ti oxide (Figure 7c) or zircon minerals. The xenotime (Figure 7c) includes significant amounts of Y (33.5 wt.%), P (15.1 wt.%), Dy (4.9 wt.%), Er (4.1 wt.%), Yb (3.8 wt. %) and Gd (1.5 wt. %), with little Si and Fe (Figure 7c). The positive relationship between Y versus HREEs (Supplementary Figure S5) of the studied granites reflects the increase in HREEs due to xenotime crystallization [7]. The existence of xenotime indicates dominant Y and P in parent magmas. The fractionation of xenotime may control on HREE distribution (e.g., [7,86]). The morphology of xenotime suggests the metasomatic origin (Figure 7c).

Parisite is an REE-bearing mineral in the Igla Ahmr alkali feldspar granites. It has been generated during hydrothermal alteration by F-rich fluids derived from the A-type magmas. Therefore, peraluminous hydrous magmas enriched in Fe may control the REE-bearing mineral formation. Parisite crystals are disseminated and can be seen on the edge of Fe-

oxides or in biotite cracks, suggesting its hydrothermal origin [8]. Allanite is found as tiny crystals exsolved along titanite in the alkali feldspar granites (Figure 7d); its morphology suggests a metasomatic origin (Figure 7d). It has high LREEs (34 wt.%) and significant contents of Ti (15.5 wt.%), Si (10.7 wt.%), Fe (5.1 wt.%), and Ca (4.2 wt.%).

In summary, rare metals and their host granites in the Igla Ahmr area are cogenetic and show characteristics of both magmatic and metasomatic origin (hybrid origin) (Figures 14c and 15). Some rare minerals in granites such as zircon, titanite, apatite, and rutile are of magmatic origin, and some of these minerals have undergone metasomatic fluid modification (such as metamict zircon). Parisite, allanite, and xenotime are of secondary origin from magma-derived fluids and/or fluid–rock interactions. The rare metals in the Igla Ahmr granites show a hybrid origin, like those found in other localities in the Eastern Desert of Egypt [4–8,11,13].

Some A-type and highly fractionated I-type granites in Egypt host rare metals in more than fourteen rare metal-bearing granitic plutons (Supplementary Figure S1), which are scattered mainly in the CED and in the northern border of SED of Egypt (e.g., [4–9,13,14]). Some granitic plutons are mineralized (e.g., Abu Dabbab granites [13] with Sn, 123–3900 ppm; Ta, 74–473 ppm and Nb, 23–165 ppm; Umm Naggat and Homrit Waggat granites [7,8] with  $\Sigma$ REEs, 187–558 ppm; Zr,s 136–431 ppm and Nb, 27–162 ppm; El-Hima granites [6] with  $\Sigma$ REEs, 176–514 ppm and Nb, 10–252 ppm; Nuweibi granites [15,16,55,83] with F, 456–1520 ppm; Ta, 40–168 ppm; Nb, 41–154 ppm and Zr, 40–104 ppm), but most of them are unmineralized; why? We found that rare metal-bearing granites have been concentrated in certain zones in the Eastern Desert (Supplementary Figure S1), and once again, we ask: why? Our observations are explained in the following section.

Based on a few other studies [6–9,11,13,56,85] in addition to this study, the rare metal mineralization in the Eastern Desert granites seems to be structurally controlled. The majority of fourteen mineralized granite plutons are found in certain zones in the CED and on the northern border of the SED of Egypt (Supplementary Figure S1) [4–7,9,11,13,15,16]. Most of these mineralized granites and their rare metal deposits were controlled by dominant NW–SE and N–S structural trends [26–28], i.e., Abu Dabbab Nb-Ta-rich granites, Sikait Nb-Ta-Li-rich granites, El-Hima garnet-REE rich granites, Umm Naggat and Homrit Waggat granites, Nuweibi granites, and Kadabora granite (Figure 1a) [4–7,9,11,13,15,16]. The NW-trending tectonic fabric is dominant in the CED, where the conjugate shear zones/faults extend in the N–S and NE–SW directions [26–28] (Figure 1a). For example, the NW–SE fault trend of the Najd shear system and related structures (N–S faults) are dominant in the studied area (Figure 1b) and may control rare metals and REE concentrations. It is not clear when Najd shearing began, although it was very active ~600 Ma [87]. Faults and fractures related to the Najd system are potential pathways for hydrothermal fluid migration and circulation; this fluid increases hydrothermal alteration of granites, and enhances mineral accumulation in a definite zone [6–8]. This fault system possibly controls gold concentrations of the Sukari gold mine and rare metals in the Abu Dabbab area [13]. There are two lines of evidence supporting our suggestion: 1-the age range of the studied granites predates Najd fault (620–540 Ma; [72]) system that is highly dominant in the CED of Egypt; 2- most of the mineralized granitic plutons in the CED are dissected by the NW–SE Najd shear zone that was conjugated with N–S faults (Figure 1a) [6–8]. The Igla Ahmr area was affected by NW–SE and N–S faults (Figure 1b), which seem to have controlled both the magma intrusion, and occurrence of rare metal-bearing granites. This is in agreement with the Barramiya shear belt (SW of the Igla Ahmr) that includes conjugate NW–SE sinistral and NE–SW dextral shears that were active c. 600 Ma [87,88].

The Najd shear zones and conjugated faults are considered as important controlling on the distribution of high rare metal contents and mineralized granitic plutons in the Eastern Desert of Egypt [6–8,12,13,87,88]. This is consistent with the study of Heikal et al. [13], who stated that the Najd fault system controlled the mineralization of rare metals in the Abu Dabbab granite pluton. In addition, the Wadi El-Hima garnet-bearing granites (up to 30 vol% of garnet; REE up to 515 ppm) are strongly affected by the NW–SE sinistral Najd fault and its conjugated NE–SW striking faults [6–8,12,13,87–90]. However, not all granites that were affected by the Najd fault system are enriched in rare metals. This may be related

to the basic components of the primitive melts (hydrous peraluminous magma with high Si and alkalis) and fluids generated from magmas, which altered primary (magmatic) minerals into secondary ones and may directly form secondary minerals (enhancing mineralization) in some granite plutons during fluid–rock interactions.

According to machine learning algorithms such as the weighted sum model and random forest, the distribution of rare metals is high in the zones of highly dense structures and in the contact between metasediments, mafic metavolcanic rocks, and metagabbrodiorite complex with granitic rocks (Figures 2 and 3). This is supported from the distribution of syenogranites and alkali feldspar granites with high REE (up to 230 ppm) contents (Figures 2 and 3; Supplementary Table S4). These granites host high Zr (up to 481.55 ppm), Nb (up to 30 ppm) and Sn contents.

From aforementioned results and discussions, the occurrence of rare metal-bearing granites in the CED of Egypt is not random (Supplementary Figure S1). There are several factors controlling the distributions of these mineralized granites in the specific region in the CED (Figure 1a). The distribution of rare metal mineralization in the Igla Ahmr granites may be attributed to: (1) essential components of primitive melts (e.g., peraluminous, rich in silica and alkalis) and magmatic-emanated fluids that enhance accumulation of rare metals in mineralized granites during rock–fluid interactions; (2) dominance of rare metal-bearing alteration zones and altered rocks related to granites such as silicification, sericitization, carbonatization, kaolinitization, and chloritization [6–8,12,89,90]; (3) increased REE and rare metal contents in more fractionated or evolved A-type and highly fractionated I-type granites; and (4) the major NW–SE structural trend (Najd trend) and conjugate N–S and NE–SW faults controlling on the distribution of rare metal-bearing granites, where these faults are considered channels for fluid circulation and rare metal accumulation.

## 8. Conclusions

1. The Igla Ahmr region in the CED of Egypt comprises rare metal-bearing syenogranites and alkali feldspar granites with subordinate tonalite xenoliths.
2. The estimated zircon temperature ( $T_{Zr}$ ) and pressure of the Igla Ahmr granites range from 717 °C to 820 °C at pressure < 4 and depth < 14 km. The oxygen fugacity of their parental magmas ranges from  $\log f_{O_2} = -15.20$  to  $-10.94$  (FMQ: +0.97 to +5.23), suggesting that our granites crystallized from calc-alkaline magmas under moderately oxidized conditions.
3. The Igla Ahmr tonalites and older syenogranite phase resemble I-type granites, which crystallized from mantle-derived magmas contaminated by crustal materials during assimilation. They are considered to be a transition between syn-collision and post-collision events in the ANS, formed at the transitional stage between the compressional and extensional tectonic setting.
4. The Igla Ahmr alkali feldspar granites and younger syenogranite phase are highly evolved peraluminous A-type granites, and enriched in Zr, Nb, Y, Th, and REEs. The A-type granites crystallized from melts after partial melting of a juvenile crustal source such as highly fractionated I-type tonalite source in the post-collisional setting during lithosphere delamination in the extensional stage. The parent magma suffered from fractional crystallization yielded syenogranites, while the more evolved magma was accompanied with copious magmatic fluids during the fractionation and crystallized as alkali feldspar granites in the late stage.
5. Rare metal-bearing minerals exist as disseminated crystals in the Igla Ahmr A-type granites and are magmatic (e.g., zircon, titanite, apatite, and rutile) and hydrothermal (parisite, allanite, and xenotime) in origin (hybrid origin). These rare metal mineralization and distribution were structurally controlled by the NW–SE Najd fault system and its conjugated faults such as N–S striking fault that enhances the accumulation of rare metals in mineralized granites during the circulation of hydrothermal fluids.

6. Based on field verification and geochemistry, the machine learning random forest algorithm yielded the most accurate mineralization prediction results, compared to the weighted sum method.
7. The distribution and high contents of rare metals in Neoproterozoic mineralized granites in the Nubian Shield may be related to several factors such as the NW–SE Najd shear zone and conjugate N–S faults, compositions of the parental melts (e.g., peraluminous, rich in silica and alkalis), compositions of magmatic-emanated fluids, and the dominant occurrence of alteration zones such as sericitization, silicification, phyllic alteration, kaolinitization, chloritization, ferrous silicate, and hydroxyl mineral alteration.

**Supplementary Materials:** The following supporting information can be downloaded at <https://www.mdpi.com/article/10.3390/min14050522/s1>: Table S1: Evidence layers representing critical and measurable features of proposed models for rare metal concentrations in the Igla Ahmr area. Table S2: EPMA of silicates (plagioclase, K-feldspar, biotite, chlorite, amphibole, magnetite, goethite, ilmenite, titanite, rutile, apatite) and rare metal-bearing minerals including monazite, tantalite, zircon, parisite, xenotime and rutile in the Gabal Igla Ahmr granites, Central Eastern Desert, Egypt. Table S3: Representative LA-ICP-MS of albite, K-feldspar and chlorite in the Igla Ahmr alkali feldspar granites. Table S4: Representative whole-rock chemistry (major Wt%, trace and REE, ppm) of the Igla Ahmr area, Central Eastern Desert, Egypt. Supplementary Figure S1. Distribution of the most important rare metal-bearing granite intrusions in the central and south Eastern Desert of Egypt. Supplementary Figure S2. (a–j) Geochemistry evidence layers using kriging interpolation. (K) Line density map of rocks in the Igla Ahmr area. (i–p) Five alteration indices of rocks in the Igla Ahmr area. Supplementary Figure S3. Harker variation diagrams of SiO<sub>2</sub> versus major elements and trace elements (Ga and Zr). Supplementary Figure S4. Variation diagrams of Zr versus FeO<sub>t</sub> (a), and ΣHREEs versus Y (b), as well as ΣREEs versus Nb (c), Zr (d), Hf (e) and Y (f) in the Igla Ahmr granites. Supplementary Figure S5. Variation diagrams of Zr (ppm) versus Hf (a), Nb/Ta (b), Ba/Rb (c) and MgO (d), as well as Nb versus Ta (e) and Y versus Ho (f) in the Igla Ahmr granites. Supplementary Figure S6. Sr versus Rb (a) and Ba versus Rb (b) diagrams, showing that fractional crystallization of plagioclase, K-feldspar and biotite played an important role in the generation of the Igla Ahmr granites.

**Author Contributions:** Conceptualization, M.Z.K.; methodology, M.Z.K., S.M.A.K., M.K.A., E.T., K.A. and Y.I.; validation, S.M.A.K. and N.H.E.-S.; formal analysis, M.Z.K., M.K.A. and E.T.; investigation, M.Z.K., S.M.A.K., N.H.E.-S. and S.M.H.; resources, M.Z.K., S.M.A.K. and N.H.E.-S.; data curation, M.Z.K., S.M.A.K. and S.M.H.; writing—original draft preparation, M.Z.K., S.M.A.K. and S.M.H.; writing—review and editing, M.Z.K.; visualization, M.Z.K. and S.M.A.K.; supervision, M.Z.K.; project administration, M.Z.K., S.M.A.K., M.K.A., E.T., N.H.E.-S., K.A. and Y.I.; funding acquisition, K.A. All authors have read and agreed to the published version of the manuscript.

**Funding:** This research was funded by Researchers Supporting Project Number (RSP2024R351), King Saud University, Riyadh, Saudi Arabia.

**Data Availability Statement:** All data derived from this research are presented in the enclosed figures and tables and two Supplementary Tables S1–S4 and Figures S1–S6.

**Acknowledgments:** The first author is grateful to all colleagues in the Geology Department at Niigata University for their support during his stay in 2019–2020 to complete polish thin sections, petrography, EDS-SEM and mineral chemistry (EPMA), and geochemical analyses of minerals and ores (LA-ICP-MS). We are grateful to the anonymous reviewers for their careful reading of our manuscript and their many insightful comments. Deep thanks and gratitude to the Researchers Supporting Project Number (RSP2024R351), King Saud University, Riyadh, Saudi Arabia, for funding this research article.

**Conflicts of Interest:** The authors declare no conflicts of interest.

## References

1. Foden, J.; Sossi, P.A.; Wawryk, C.M. Fe isotopes and the contrasting petrogenesis of A-, I- and S-type granite. *Lithos* **2015**, *212*, 32–44. [\[CrossRef\]](#)
2. Pearce, J.A.; Harris, N.B.W.; Tindle, A.G. Trace Element Discrimination Diagrams for the Tectonic Interpretation of Granitic Rocks. *J. Petrol.* **1984**, *25*, 956–983. [\[CrossRef\]](#)
3. El-Bialy, M.Z.; Omar, M.M. Spatial association of Neoproterozoic continental arc I-type and post-collision A-type granitoids in the Arabian–Nubian Shield: The Wadi Al-Baroud Older and Younger Granites, North Eastern Desert, Egypt. *J. Afr. Earth Sci.* **2015**, *103*, 1–29. [\[CrossRef\]](#)
4. Sami, M.; Ntaflos, T.; Farahat, E.S.; Mohamed, H.A.; Ahmed, A.F.; Hauzenberger, C. Mineralogical, geochemical and Sr-Nd isotopes characteristics of fluorite-bearing granites in the Northern Arabian–Nubian Shield, Egypt: Constraints on petrogenesis and evolution of their associated rare metal mineralization. *Ore Geol. Rev.* **2017**, *88*, 1–22. [\[CrossRef\]](#)
5. Azer, M.K.; Abdelfadil, K.M.; Asimow, P.D.; Khalil, A.E. Tracking the transition from subduction-related to post-collisional magmatism in the north Arabian–Nubian Shield: A case study from the Homrit Waggat area of the Eastern Desert of Egypt. *Geol. J.* **2020**, *55*, 4426–4452. [\[CrossRef\]](#)
6. Khedr, M.Z.; Abo Khashaba, S.M.; El-Shibiny, N.H.; El-Arafy, R.A.; Takazawa, E.; Azer, M.K.; Pallin, M. Remote sensing techniques and geochemical constraints on the formation of the Wadi El-Hima mineralized granites, Egypt: New insights into the genesis and accumulation of garnets. *Int. J. Earth Sci.* **2022**, *111*, 2409–2443. [\[CrossRef\]](#)
7. Khedr, M.Z.; Khashaba, S.M.A.; El-Shibiny, N.H.; Takazawa, E.; Hassan, S.M.; Azer, M.K.; Whattam, S.A.; El-Arafy, R.A.; Ichiyama, Y. Integration of remote sensing and geochemical data to characterize mineralized A-type granites, Egypt: Implications for origin and concentration of rare metals. *Int. J. Earth Sci.* **2023**, *112*, 1717–1745. [\[CrossRef\]](#)
8. Abo Khashaba, S.M.; El-Shibiny, N.H.; Hassan, S.M.; Takazawa, E.; Khedr, M.Z. Application of remote sensing data integration in detecting mineralized granitic zones: A case study of the Iгла Ahmr, Central Eastern Desert, Egypt. *J. Afr. Earth Sci.* **2023**, *200*, 104855. [\[CrossRef\]](#)
9. Stern, J.R.; Khedr, Z.M.; Whitehouse, M.J.; Romer, R.L.; Abo Khashaba, S.M.; El-Shibiny, N.H. Late Cryogenian and early Ediacaran rare-metal rich granites in the Eastern Desert of Egypt: Constraints from zircon ages and whole-rock Sr- and Nd- and feldspar Pb-isotopic compositions. *J. Geol. Soc.* **2024**, *181*, jgs2023–jgs2068. [\[CrossRef\]](#)
10. Gahlan, H.A.; Azer, M.K.; Al-Hashim, M.H.; Heikal, M.T.S. Highly evolved rare-metal bearing granite overprinted by alkali metasomatism in the Arabian Shield: A case study from the Jabal Tawlah granites. *J. Afr. Earth Sci.* **2022**, *192*, 104556. [\[CrossRef\]](#)
11. Seddik, A.M.; Darwish, M.H.; Azer, M.K.; Asimow, P.D. Assessment of magmatic versus post-magmatic processes in the Mueilha rare-metal granite, Eastern Desert of Egypt, Arabian–Nubian Shield. *Lithos* **2020**, *366*, 105542. [\[CrossRef\]](#)
12. El-Hadek, H.H.; Mohamed, M.A.; El-Habaak, G.H.; Bishara, W.W.; Ali, K.A. Geochemical constraints on petrogenesis of Homrit Waggat rare metal granite, Egypt. *Int. J. Geophys. Geochem.* **2016**, *3*, 33–48.
13. Heikal, M.T.S.; Khedr, M.Z.; El-Monesf, M.A.; Gomaa, S.R. Petrogenesis and geodynamic evolution of Neoproterozoic Abu Dabbab Albite Granite, Central Eastern Desert of Egypt: Petrological and geochemical constraints. *J. Afr. Earth Sci.* **2019**, *158*, 103518. [\[CrossRef\]](#)
14. Zoheir, B.; Lehmann, B.; Emam, A.; Radwan, A.; Zhang, R.; Bain, W.M.; Steele-MacInnis, M.; Nolte, N. Extreme fractionation and magmatic hydrothermal transition in the formation of the Abu Dabbab rare-metal granite, Eastern Desert, Egypt. *Lithos* **2020**, *352*, 105329. [\[CrossRef\]](#)
15. Helba, H.; Trumbull, R.B.; Morteani, G.; Khalil, S.O.; Arslan, A. Geochemical and petrographic studies of Ta mineralization in the Nuweibi albite granite complex, Eastern Desert, Egypt. *Miner. Depos.* **1997**, *32*, 164–179. [\[CrossRef\]](#)
16. Abou El Maaty, M.A.; Ali Bik, M.W. Petrology of alkali feldspar granite of Nuweibi and Gebel El-Mueilha, central Eastern Desert, Egypt. *Egypt. J. Geol.* **2000**, *44*, 127–148.
17. Whalen, J.B.; Currie, K.L.; Chappell, B.W. A-type granites: Geochemical characteristics, discrimination and petrogenesis. *Contrib. Mineral. Petrol.* **1987**, *95*, 407–419. [\[CrossRef\]](#)
18. Chappell, B.W.; White, A.J.R. I- and S-type granites in the Lachlan Fold Belt. *Earth Environ. Sci. Trans. R. Soc. Edinb.* **1992**, *83*, 1–26.
19. King, P.L.; White, A.J.R.; Chappell, B.W.; Allen, C.M. Characterization and origin of aluminous A-type granites from the Lachlan Fold Belt, southeastern Australia. *J. Petrol.* **1997**, *38*, 371–391. [\[CrossRef\]](#)
20. Champion, D.C.; Chappell, B.W. Petrogenesis of felsic I-type granites: An example from northern Queensland. *Earth Environ. Sci. Trans. R. Soc. Edinb.* **1992**, *83*, 115–126.
21. Rodriguez-Galiano, V.; Sanchez-Castillo, M.; Chica-Olmo, M.; Chica-Rivas, M.J.O.G.R. Machine learning predictive models for mineral prospectivity: An evaluation of neural networks, random forest, regression trees and support vector machines. *Ore Geol. Rev.* **2015**, *71*, 804–818. [\[CrossRef\]](#)
22. Chen, Y.; Wu, W. Mapping mineral prospectivity using an extreme learning machine regression. *Ore Geol. Rev.* **2017**, *80*, 200–213. [\[CrossRef\]](#)
23. Pradhan, B.; Jena, R.; Talukdar, D.; Mohanty, M.; Sahu, B.K.; Raul, A.K.; Abdul Maulud, K.N. A New Method to Evaluate Gold Mineralisation-Potential Mapping Using Deep Learning and an Explainable Artificial Intelligence (XAI) Model. *Remote Sens.* **2022**, *14*, 4486. [\[CrossRef\]](#)
24. Brown, W.M.; Gedeon, T.D.; Groves, D.I.; Barnes, R.G. Artificial neural networks: A new method for mineral prospectivity mapping. *Aust. J. Earth. Sci.* **2000**, *47*, 757–770. [\[CrossRef\]](#)

25. Johnson, P.R.; Andresen, A.; Collins, A.S.; Fowler, A.R.; Fritz, H.; Ghebreab, W.; Kusky, T.; Stern, R.J. Late Cryogenian–Ediacaran history of the Arabian–Nubian Shield: A review of depositional, plutonic, structural, and tectonic events in the closing stages of the northern East African Orogen. *J. Afr. Earth Sci.* **2011**, *61*, 167–232. [[CrossRef](#)]
26. Greiling, R.O.; Abdeen, M.M.; Dardir, A.A.; El Akhal, H.; El Ramly, M.F.; Kamal El Din, G.M.; Osman, A.F.; Rashwan, A.A.; Rice, A.H.; Sadek, M.F. A structural synthesis of the Proterozoic Arabian–Nubian Shield in Egypt. *Geol. Rundsch.* **1994**, *83*, 484–501. [[CrossRef](#)]
27. Fritz, H.; Wallbrecher, E.; Khudier, A.A.; Abu El-Ela, F.; Dallmeyer, R.D. Formation of Neoproterozoic metamorphic core complexes during oblique convergence, Eastern Desert, Egypt. *J. Afr. Earth Sci.* **1996**, *23*, 311–329. [[CrossRef](#)]
28. Abd El-Wahed, M.A. Oppositely dipping thrusts and transpressional imbricate zone in the Central Eastern Desert of Egypt. *J. Afr. Earth Sci.* **2014**, *100*, 42–59. [[CrossRef](#)]
29. Stern, R.J.; Ali, K. Crustal evolution of the Egyptian Precambrian rocks. In *The Geology of Egypt*; Springer: Cham, Switzerland, 2020; pp. 131–151.
30. EGSMA. *Geological Maps of Marsa Alam 1:100,000 Scale*; The Egyptian Geologic Survey and Mining Authority (EGSMA): Abbasiya, Cairo, 1991; Sheet 1.
31. Breiman, L. Random forests. *Mach. Learn.* **2001**, *45*, 5–32. [[CrossRef](#)]
32. Carranza, E.J.M.; Laborte, A.G. Random forest predictive modeling of mineral prospectivity with small number of prospects and data with missing values in Abra (Philippines). *Comput. Geosci.* **2015**, *74*, 60–70. [[CrossRef](#)]
33. Shebl, A.; Abriha, D.; Fahil, A.S.; El-Dokouny, H.A.; Elrasheed, A.A.; Csámer, Á. PRISMA hyperspectral data for lithological mapping in the Egyptian Eastern Desert: Evaluating the Support Vector Machine, Random Forest, and XG Boost Machine Learning Algorithms. *Ore Geol. Rev.* **2023**, *161*, 105652. [[CrossRef](#)]
34. Deer, W.A.; Howie, R.A.; Zussman, J. *An Introduction to Rock-Forming Minerals*, 2nd ed.; Longmans: London, UK, 1992; p. 517.
35. Nachit, H.; Ibhi, A.; Ohoud, M.B. Discrimination between primary magmatic biotites, reequilibrated biotites and neofomed biotites. *Comptes Rendus Geosci.* **2005**, *337*, 1415–1420. [[CrossRef](#)]
36. Abdel-Rahman, A.F.M. Nature of biotites from alkaline, calc-alkaline, and peraluminous magmas. *J. Petrol.* **1994**, *35*, 525–541. [[CrossRef](#)]
37. Leake, B.E.; Woolley, A.R.; Arps, C.E.; Birch, W.D.; Gilbert, M.C.; Grice, J.D.; Hawthorne, F.C.; Kato, A.; Kisch, H.J.; Krivovichev, V.G.; et al. Nomenclature of amphiboles; report of the subcommittee on amphiboles of the International Mineralogical Association, Commission on New Minerals and Mineral Names. *Am. Mineral.* **1997**, *35*, 219–246.
38. Hey, M.H. A new review of chlorites. *Mineral. Mag.* **1954**, *30*, 278–292. [[CrossRef](#)]
39. Sun, S.S.; McDonough, W.F. Chemical and isotopic systematics of oceanic basalts: Implications for mantle composition and processes. *Geol. Soc. Spec. Publ.* **1989**, *42*, 313–345. [[CrossRef](#)]
40. Rudnick, R.L.; Fountain, D.M. Nature and composition of the continental crust: A lower crustal perspective. *Rev. Geophys.* **1995**, *33*, 267–309. [[CrossRef](#)]
41. De la Roche, H.D.; Letierrier, J.T.; Grandclaude, P.; Marchal, M. A classification of volcanic and plutonic rocks using R1-R2-diagram and major-element analyses—Its relationships with current nomenclature. *Chem. Geol.* **1980**, *29*, 183–210. [[CrossRef](#)]
42. Gad, S.; Kusky, T. ASTER spectral ratioing for lithological mapping in the Arabian–Nubian Shield, the Neoproterozoic Wadi Kid area, Sinai, Egypt. *Gondwana Res.* **2007**, *11*, 326–335. [[CrossRef](#)]
43. Pour, A.B.; Hashim, M.; Hong, J.K.; Park, Y. Lithological and alteration mineral mapping in poorly exposed lithologies using Landsat-8 and ASTER satellite data: North-Eastern Graham Land, Antarctic Peninsula. *Ore Geol. Rev.* **2019**, *108*, 112–133. [[CrossRef](#)]
44. Hassan, S.M.; Youssef, M.A.; Gabr, S.; Sadek, M.F. Radioactive mineralization detection using remote sensing and airborne gamma-ray spectrometry at Wadi Al-Miyah area, Central Eastern Desert, Egypt. *Egypt. J. Remote Sens. Space Sci.* **2022**, *25*, 37–53. [[CrossRef](#)]
45. Sun, T.; Chen, F.; Zhong, L.; Liu, W.; Wang, Y. GIS-based mineral prospectivity mapping using machine learning methods: A case study from Tongling ore district, eastern China. *Ore Geol. Rev.* **2019**, *109*, 26–49. [[CrossRef](#)]
46. Boehnke, P.; Watson, E.B.; Trail, D.; Harrison, T.M.; Schmitt, A.K. Zircon saturation re-revisited. *Chem. Geol.* **2013**, *351*, 324–334. [[CrossRef](#)]
47. Yang, X.M. Estimation of crystallization pressure of granite intrusions. *Lithos* **2017**, *286*, 324–329. [[CrossRef](#)]
48. Manning, D.A.C. The effect of fluorine on liquidus phase relationships in the system Qz-Ab-Or with excess water at 1 kb. *Contrib. Mineral. Petrol.* **1981**, *76*, 206–215. [[CrossRef](#)]
49. Wones, D.R. Significance of the assemblage titanite + magnetite + quartz in granitic-rocks. *Am. Mineral.* **1989**, *74*, 744–749.
50. Sylvester, P.J. Post-collisional alkaline granites. *J. Geol.* **1989**, *97*, 261–280. [[CrossRef](#)]
51. Frost, B.R.; Barnes, C.G.; Collins, W.J.; Arculus, R.J.; Ellis, D.J.; Frost, C.D. A geochemical classification for granitic rocks. *J. Petrol.* **2001**, *42*, 2033–2048. [[CrossRef](#)]
52. Eby, G.N. Chemical subdivision of the A-type granitoids: Petrogenetic and tectonic implications. *Geology* **1992**, *20*, 641–644. [[CrossRef](#)]
53. Farahat, E.S.; Zaki, R.; Hauzenberger, C.; Sami, M. Neoproterozoic calc-alkaline peraluminous granitoids of the Deleihimmi pluton, Central Eastern Desert, Egypt: Implications for transition from late-to post-collisional tectonomagmatic evolution in the northern Arabian–Nubian Shield. *Geol. J.* **2011**, *46*, 544–560. [[CrossRef](#)]

54. Maniar, P.D.; Piccoli, P.M. Tectonic discrimination of granitoids. *Geol. Soc. Am. Bull.* **1989**, *101*, 635–643. [[CrossRef](#)]
55. Moussa, H.E.; Asimow, P.D.; Azer, M.K.; Abou El Maaty, M.A.; Akarish, A.I.; Yanni, N.N.; Mubarak, H.S.; Wilner, M.J.; Elsaheer, M.A. Magmatic and hydrothermal evolution of highly-fractionated rare-metal granites at Gabal Nuweibi, Eastern Desert, Egypt. *Lithos* **2021**, *400*, 106405. [[CrossRef](#)]
56. Abuamarah, B.A.; Azer, M.K.; Asimow, P.D.; Ghrefat, H.; Mubarak, H.S. Geochemistry and petrogenesis of late Ediacaran rare-metal albite granites of the Arabian-Nubian Shield. *Acta Geol. Sin. Engl. Ed.* **2021**, *95*, 459–480. [[CrossRef](#)]
57. Pearce, J.A. Sources and settings of granitic rocks. *Episodes* **1996**, *19*, 120–125. [[CrossRef](#)]
58. Batchelor, R.A.; Bowden, P. Petrogenetic interpretation of granitoid rock series using multicationic parameters. *Chem. Geol.* **1985**, *48*, 43–55. [[CrossRef](#)]
59. Hassan, M.A.; Hashad, A.H. Precambrian of Egypt. In *The Geology of Egypt*; Said, R., Ed.; Balkema: Rotterdam, The Netherlands, 1990; pp. 201–245.
60. Barker, F.; Arth, J.G. Generation of trondhjemitic-tonalitic liquids and Archean bimodal trondhjemite-basalt suites. *Geology* **1976**, *4*, 596–600. [[CrossRef](#)]
61. Huang, X.L.; Zhong, J.W.; Xu, Y.G. Two tales of the continental lithospheric mantle prior to the destruction of the North China Craton: Insights from Early Cretaceous mafic intrusions in western Shandong, East China. *Geochim. Cosmochim. Acta* **2012**, *96*, 193–214. [[CrossRef](#)]
62. DePaolo, D.J. Trace element and isotopic effects of combined wall rock assimilation and fractional crystallization. *Earth Planet. Sci. Lett.* **1981**, *53*, 189–202. [[CrossRef](#)]
63. Laurent, O.; Martin, H.; Moyen, J.F.; Doucelance, R. The diversity and evolution of late-Archean granitoids: Evidence for the onset of “modern-style” plate tectonics between 3.0 and 2.5 Ga. *Lithos* **2014**, *205*, 208–235. [[CrossRef](#)]
64. Akinin, V.V.; Miller, E.L.; Wooden, J.L. Petrology and geochronology of crustal xenoliths from the Bering Strait region: Linking deep and shallow processes in extending continental crust. Crustal cross sections from the western North American Cordillera and elsewhere: Implications for tectonic and petrologic processes. *Geol. Soc. Am.* **2009**, *456*, 39–68.
65. Taylor, S.R.; McLennan, S.M. The continental crust: Its composition and evolution. *Geol. Mag.* **1985**, *122*, 673–674.
66. Smirnov, V.I.; Ginzburg, A.I.; Grigoriev, V.M.; Yakovlev, G.F. *Studies of Mineral Deposits*; Mir Publishers: Moscow, Russia, 1983; p. 450.
67. Garcia, D.; Fonteilles, M.; Moutte, J. Sedimentary fractionations between Al, Ti, and Zr and the genesis of strongly peraluminous granites. *J. Geol.* **1994**, *102*, 411–422. [[CrossRef](#)]
68. Moghazi, A.M.; Mohamed, F.H.; Kanisawa, S. Geochemical and petrological evidence of calc-alkaline and A-type magmatism in the Homrit Waggat and El-Yatima areas of eastern Egypt. *J. Afr. Earth Sci.* **1999**, *29*, 535–549. [[CrossRef](#)]
69. Petford, N.; Gallagher, K. Partial melting of mafic (amphibolitic) lower crust by periodic influx of basaltic magma. *Earth Planet. Sci. Lett.* **2001**, *193*, 483–499. [[CrossRef](#)]
70. Nicolae, I.; Saccani, E. Petrology and geochemistry of the Late Jurassic calc-alkaline series associated to Middle Jurassic ophiolites in the South Apuseni Mountains (Romania). *Swiss Bull. Mineral. Petrol.* **2003**, *83*, 81–96.
71. Patiño Douce, A.E. Generation of metaluminous A-type granites by low-pressure melting of calc-alkaline granitoids. *Geology* **1997**, *25*, 743–746. [[CrossRef](#)]
72. Robinson, F.A.; Bonin, B.; Pease, V.; Anderson, J.L. A discussion on the tectonic implications of Ediacaran late- to post-orogenic A-type granite in the northeastern Arabian Shield, Saudi Arabia. *Tectonics* **2017**, *36*, 582–600. [[CrossRef](#)]
73. Holtz, F.; Behrens, H.; Dingwell, D.B.; Taylor, R.P. Water solubility in aluminosilicate melts of haplogranite composition at 2 kbar. *Chem. Geol.* **1992**, *96*, 289–302. [[CrossRef](#)]
74. Mansour, S.; Hasebe, N.; Meert, J.; Tamura, A.; Khalaf, F.I.; El-Shafei, M.K. Evolution of the Arabian-Nubian Shield in Gabal Samra area, Sinai; implications from zircon U–Pb geochronology. *J. Afr. Earth Sci.* **2022**, *192*, 104538. [[CrossRef](#)]
75. Ali, K.A.; Surour, A.A.; Whitehouse, M.J.; Andresen, A. Single zircon Hf–O isotope constraints on the origin of A-type granites from the Jabal Al-Hassir ring complex, Saudi Arabia. *Precambrian Res.* **2015**, *256*, 131–147. [[CrossRef](#)]
76. Ali, K.A.; Moghazi, A.K.M.; Maurice, A.E.; Omar, S.A.; Wang, Q.; Wilde, S.A.; Moussa, E.M.; Manton, W.I.; Stern, R.J. Composition, age, and origin of the ~620 Ma Humr Akarim and Humrat Mukbid A-type granites: No evidence for pre-Neoproterozoic basement in the Eastern Desert, Egypt. *Int. J. Earth Sci.* **2012**, *101*, 1705–1722. [[CrossRef](#)]
77. Eliwa, H.A.; Breikreuz, C.; Murata, M.; Khalaf, I.M.; Bühler, B.; Itaya, T.; Takahashi, T.; Hirahara, Y.; Miyazaki, T.; Kimura, J.I.; et al. SIMS zircon U–Pb and mica K–Ar geochronology, and Sr–Nd isotope geochemistry of Neoproterozoic granitoids and their bearing on the evolution of the north Eastern Desert, Egypt. *Gondwana Res.* **2014**, *25*, 1570–1598. [[CrossRef](#)]
78. Li, Z.H.; Liu, M.; Gerya, T. Lithosphere delamination in continental collisional orogens: A systematic numerical study. *J. Geophys. Res. Solid.* **2016**, *121*, 5186–5211. [[CrossRef](#)]
79. Azer, M.K.; Asimow, P.D. Petrogenetic evolution of the Neoproterozoic igneous rocks of Egypt. In *The Geology of the Egyptian Nubian Shield*; Springer: Berlin/Heidelberg, Germany, 2021; pp. 343–382. [[CrossRef](#)]
80. Melcher, F.; Graupner, T.; Gäbler, H.E.; Sitnikova, M.; Henjes-Kunst, F.; Oberthür, T.; Gerdes, A.; Dewaele, S. Tantalum–(niobium–tin) mineralisation in African pegmatites and rare metal granites: Constraints from Ta–Nb oxide mineralogy, geochemistry and U–Pb geochronology. *Ore Geol. Rev.* **2015**, *64*, 667–719. [[CrossRef](#)]
81. Creaser, R.A.; Price, R.C.; Wormald, R.J. A-type granites revisited: Assessment of a residual-source model. *Geology* **1991**, *19*, 163–166. [[CrossRef](#)]

82. Ghoneim, M.F.; Lebda, E.M.; Nasr, B.B.; Khedr, M.Z. Geology and tectonic evolution of the area around wadi Arais, southern Eastern Desert, Egypt. In Proceedings of the 6th International Conference on the Geology of the Arab World (GAW6), Cairo, Egypt, 12 February 2002; Volume 1, pp. 45–66.
83. Kamel, O.A.; El Tabbal, H.K. Petrology and mineralogy of Nuweibi and Abu Dabbab rare metal apogranites, Eastern Desert, Egypt. In Proceedings of the International Symposium Geodynamic Evolution of the Afro-Arabian Rift System, Rome, Italy, 18–20 April 1980; Volume 47, pp. 685–705.
84. El-Galy, M.M.; Khaleal, F.M.; Bakhit, A.F. Comparative study on the geological and geochemical characteristics of some rare-metal granites, south Eastern Desert, Egypt. *Nucl. Sci. Sci. J.* **2016**, *5*, 109–120.
85. Abuamarah, B.A.; Azer, M.K.; Seddik, A.M.; Asimow, P.D.; Guzman, P.; Fultz, B.T.; Wilner, M.J.; Dalleska, N.; Darwish, M.H. Magmatic and post-magmatic evolution of post-collisional rare-metal bearing granite: The Neoproterozoic Homrit Akarem Granitic Intrusion, south Eastern Desert of Egypt, Arabian-Nubian Shield. *Geochemistry* **2022**, *82*, 125840. [[CrossRef](#)]
86. Pérez-Soba, C.; Villaseca, C. Petrogenesis of highly fractionated I-type peraluminous granites: La Pedriza pluton (Spanish Central System). *Geol. Acta* **2010**, *8*, 131–149.
87. Hamimi, Z.; Abd El-Wahed, M.A. Suture(s) and Major Shear Zones in the Neoproterozoic Basement of Egypt. In *The Geology of Egypt, Regional Geology Reviews*; Hamimi, Z., El-Barkooky, A., Martínez Frías, J., Fritz, H., Abd El-Rahman, Y., Eds.; Springer Nature: Cham, Switzerland, 2020; Chapter 5; pp. 153–189.
88. Abd El-Wahed, M.A.; Harraz, H.; El-Behairy, M.H. Transpressional imbricate thrust zones controlling gold mineralization in the Central Eastern Desert of Egypt. *Ore Geol. Rev.* **2016**, *78*, 424–446. [[CrossRef](#)]
89. Abdelkader, M.A.; Watanabe, Y.; Shebl, A.; El-Dokouny, H.A.; Dawoud, M.; Csámer, Á. Effective delineation of rare metal-bearing granites from remote sensing data using machine learning methods: A case study from the Umm Naggat Area, Central Eastern Desert, Egypt. *Ore Geol. Rev.* **2022**, *150*, 105184. [[CrossRef](#)]
90. El-Afandy, A.H.; Abdalla, H.M.; Aly, M.M.; Ammar, F. Geochemistry and radioactive potentiality of Um Naggat apogranite, central eastern desert, Egypt. *Resour. Geol.* **2000**, *50*, 39–51. [[CrossRef](#)]

**Disclaimer/Publisher’s Note:** The statements, opinions and data contained in all publications are solely those of the individual author(s) and contributor(s) and not of MDPI and/or the editor(s). MDPI and/or the editor(s) disclaim responsibility for any injury to people or property resulting from any ideas, methods, instructions or products referred to in the content.